Atmos. Chem. Phys., 25, 6325–6352, 2025
https://doi.org/10.5194/acp-25-6325-2025

Atmospheric Chemistry and Physics
Open Access
EGU

Research article

Phase matrix characterization of long-range-transported Saharan dust using multiwavelength-polarized polar imaging nephelometry

Elena Bazo[1,2], Daniel Pérez-Ramírez[1,2], Antonio Valenzuela[1,2], J. Vanderlei Martins[3], Gloria Titos[1,2], Alberto Cazorla[1,2], Fernando Rejano[1,4], Diego Patrón[1,2], Arlett Díaz-Zurita[1,2], Francisco José García-Izquierdo[5], David Fuertes[4], Lucas Alados-Arboledas[1,2], and Francisco José Olmo[1,2]

[1]Andalusian Institute for Earth System Research (IISTA-CEAMA), Granada 18006, Spain
[2]Department of Applied Physics, University of Granada, Granada 18071, Spain
[3]Department of Physics and Earth and Space Institute, University of Maryland, Baltimore County, Baltimore, Maryland, USA
[4]GRASP-SAS, Remote Sensing Developments, Lille, France
[5]Instituto de Astrofísica de Andalucía (IAA-CSIC), Granada 18008, Spain

Correspondence: Daniel Pérez-Ramírez (dperez@ugr.es)

Received: 5 July 2024 – Discussion started: 14 August 2024
Revised: 26 February 2025 – Accepted: 10 March 2025 – Published: 26 June 2025

Abstract. This work investigates scattering matrix elements during different Saharan dust outbreaks over Granada (southeast Spain) in 2022 using a polarized imaging nephelometer (PI-Neph) capable of measuring continuously the phase function (F_{11}) and the polarized phase function ($-F_{12}/F_{11}$) at three different wavelengths (405, 515 and 660 nm) in the range 5–175°. The focus is on two extreme dust events ($PM_{10} > 1000\,\mu g\,m^{-3}$) in March 2022. During the peaks of these events F_{11} and $-F_{12}/F_{11}$ show the classical patterns observed for dust samples in laboratory measurements available in the Granada–Amsterdam Light Scattering Database at all wavelengths. However, for the moments prior to and after the peaks the results reveal important sensitivity in $-F_{12}/F_{11}$ at 405 nm. For the other wavelengths, however, this difference in $-F_{12}/F_{11}$ is not evident. Moreover, no remarkable changes are found in F_{11}, which is always characterized by strong predominance of forward scattering. The analyses of more frequent and moderate events recorded in summer 2022 (PM_{10} between 50 and $100\,\mu g\,m^{-3}$) revealed F_{11} and $-F_{12}/F_{11}$ patterns like those observed prior to and after the extreme events. The combination of PI-Neph measurements with additional in situ instrumentation allowed a typing classification that revealed the peaks in the extreme dust events as pure dust, while for the rest of cases it remarked a mixture of dust with urban background pollution. In addition, simulations with the Generalized Retrieval of Atmosphere and Surface Properties (GRASP) code explain the different patterns in $-F_{12}/F_{11}$, with changes in the refractive indexes and with the different contributions of the fine and coarse mode.

1 Introduction

The imprecise determination of atmospheric aerosol microphysical properties is currently the main source of uncertainty in climate projections, as stated by the latest Intergovernmental Panel on Climate Change (IPCC; Forster et al., 2021). Particularly, aerosol particles can scatter and absorb solar radiation, known as the direct effect (Haywood and Boucher, 2000). Moreover, aerosol particles can interact with clouds in different ways: aerosol absorption can modify the energy balance in the atmosphere, affecting cloud development and properties (the semi-direct effect, Fan et al., 2016). They can also serve as cloud condensation nuclei (CCN) and ice-nucleating particles (INPs) upon which cloud droplets and ice crystals form (the aerosol indirect effect on clouds, Rosenfeld et al. 2014).

Advancing aerosol knowledge faces complex challenges due to the large variability of aerosol types and to aerosol sources and transformation processes in the atmosphere during their transport. More specifically, mineral dust is the most important source of primary particles in the atmosphere, with an estimated emission rate of 1000–3000 $\mathrm{Tg\,yr^{-1}}$, representing about half of the annual particle mass emission at the global scale (Kok et al., 2021). Mineral dust sources extend over a wide area on the planet highlighting the global dust belt that extends from the arid regions of the west coast of northern Africa through the Middle East and central Asia. Such a belt includes the Sahara, which is the largest in the world, responsible for almost 50 % of the global dust emissions (Kok et al., 2017). In this sense, recent studies (Kok et al., 2018) estimate the direct dust–climate feedback parameter associated with the direct radiative effect in the range -0.04 to $+0.02\,\mathrm{W\,m^{-2}\,{}^{\circ}C^{-1}}$ (net, short and long wavelength) but being highly dependent on the model used. The problem with understanding the role of dust in climate becomes even more complex due to the changes in arid lands since the pre-industrial era, which are producing an increase of global dust mass loading (Kok et al., 2017). Most of these uncertainties are due to the challenges in better understanding mineral dust composition and variability with size and sources (Gonçalves Ageitos et al., 2023).

Mineral dust particles are typically considered as large particles in the coarse (1–10 µm) and super-coarse (> 10 µm) modes (Renard et al., 2018), although recent studies have also shown the presence of a fine mode (ranges below 1 µm diameter) in mineral dust (Huang et al., 2019). The current discrepancies about the roles of fine, coarse and super-coarse modes in the dust sample (González-Flórez et al., 2023) imply difficulties in dust modeling that add uncertainties to the climate modeling (Adebiyi and Kok, 2020). One critical point is the modeling of coarse mode because of the non-sphericity of these types of particles (Mischenko et al., 2002) and also inferring the complex refractive index (Formenti et al., 2003) that ultimately depends on particle size, shape and chemical composition (González-Romero et al., 2023). For example, iron oxides are the key to understanding the mineral dust absorption properties in the UV (e.g., hematite, goethite), whilst Ca-rich carbonates become important in the infrared region (Formenti et al., 2014). These variabilities in size-related and absorption parameters make it difficult to model the response of mineral dust to the direct radiative effect accurately (Adebiyi et al., 2023). The problem becomes even more complex because of the interactions of dust particles with other precursor gases and aerosol particles already present in the atmosphere (Ooki and Uematsu, 2005). For example, the variabilities in dust size, shape and chemical composition are also related to emerging questions such as the role of big mineral dust particles in new particle formation in the atmosphere (Casquero-Vera et al., 2023).

Remote sensing techniques are widely used to infer dust properties. For example, passive remote sensing techniques such as sun photometry in the Aerosol Robotic Network (AERONET; Holben et al., 1998) or star/moon photometry (i.e., Pérez-Ramírez et al., 2008, 2011; Berkoff et al., 2011) allow us to have a representation of column-integrated values, particularly aerosol optical depth (AOD). But to infer other aerosol optical (e.g., aerosol complex refractive index and single scattering albedo) and microphysical (e.g., aerosol size distribution) properties, it is necessary to solve ill-posed problems for which the information content is low (Dubovik and King, 2000; King et al., 1978; Nakajima et al., 1996; Olmo et al., 2006, 2008; Pérez-Ramírez et al., 2015). These algorithms use the Mie theory for the internal computation of particles phase functions, but in the case of dust particles, more complex approaches such as the T-matrix method are needed because of the non-sphericity of dust particles (Mischenko and Travis, 1994, 1997) . Nevertheless, several inversion algorithms have been developed incorporating T-matrix modeling, as it is one of the most popular algorithms developed within the AERONET network (Dubovik et al., 2006).

Ground-based remote sensing techniques are only representative of the measurement site, and to face these limitations satellite measurements are ideal because they can cover wide regions of the world. However, passive remote sensing space platforms deal with additional complexity in the retrieval of aerosol properties because of the influence of surface reflectance (Kahn et al., 1988; Levy et al., 2007). The simplest retrievals use look-up tables with a priori aerosol types with great success in obtaining AOD but limited capacity for obtaining other aerosol parameters because of the difficulties in separating the signals corresponding to the atmosphere and surface (Dubovik et al., 2019). To solve these limitations, the use of multiwavelength and multi-angle polarization measurements is ideal to improve the information content (Mishchenko et al., 2007). Some of the first polarized-based measurements for aerosol studies were carried out by the POLDER instrument (POlarization and Directionality of the Earth's Reflectances; Deuzé et al., 1993) that acquired 9 years of data. These measurements were used as inputs in the Generalized Retrieval of Atmosphere and Surface Properties algorithm (GRASP, Dubovik et al., 2014, 2021) for obtaining extended aerosol optical and microphysical properties. Algorithms such as GRASP are becoming the operational algorithms in new satellite missions (Remer et al., 2019; GAPMAP, 2025; Hasekamp et al., 2024), but these algorithms need phase matrix measurements for optimizing the kernels used internally, particularly for non-spherical particles.

The main difficulties in measuring aerosol phase matrix of ambient air lie in the design and development of appropriate polar nephelometry capable of measuring light scattered with appropriate angular resolution. The first polar nephelometry developments were based on moveable detectors, but they must be mechanically stable and require a constant population of aerosol particles that does not change appreciably during the detector sweep (Holland and Gagne, 1970; Hovenier et al., 2003; Jaggard et al., 1981; Kuik et al., 1991; Perry et al., 1978; Volten et al., 2001). Other polar nephelometry designs use arrays of many detectors placed on representative scattering angles (Barkey et al., 1999; Gayet et al., 1998; Pope et al., 1992; West et al., 1997; Wyatt et al., 1988), but this technique requires careful calibration of the detectors and generally suffers from low angular resolution ($\sim 2°$). These instrumental limitations have implied that the usual study of scattering matrix elements of dust particles is done in the laboratory for synthetic samples of minerals that compose dust particles (Curtis et al., 2008; Huang et al., 2020; Meland et al., 2010; Muñoz et al., 2010a; Renard et al., 2014, 2010) or with collected dust samples (Muñoz et al., 2007a; Renard et al., 2014, 2010, 2024). Actually, the parametrizations of the mineral dust phase matrix used for the AERONET algorithm were calculated by fitting the laboratory measurements of different non-spherical particles samples (i.e., Dubovik et al., 2006). Such measurements were performed at a few wavelengths, and what is more important, they might be non-representative of real aerosol measurements because of the different transformations and interactions of dust particles since they were emitted in their source regions. There is therefore a current challenge in having an extended database of measurements of dust phase matrix elements for different dust types and mixtures, particularly at different stages of dust evolution after their emission from the remote desert areas.

The latest developments use imaging techniques (Bian et al., 2017; Curtis et al., 2007; Dolgos and Martins, 2014) to determine the phase matrix with a single detector and a relatively compact design that does not require moveable parts. The polarized imaging nephelometer (PI-Neph) was one of the first designs of a polar nephelometer that used imaging techniques, developed by the University of Maryland, Baltimore County (UMBC). This first prototype of the PI-Neph could acquire the aerosol phase matrix at 473, 532 and 671 nm with 0.5° resolution. The instrument was deployed on the NASA DC8 aircraft and operated during special field campaigns (Espinosa et al., 2018; Reed Espinosa et al., 2017). Other PI-Neph instruments based on the first UMBC design are operated by NOAA (Ahern et al., 2022; Manfred et al., 2018). The main novelty of these prototypes is that they measure phase matrix elements of ambient air, where conditions can be very different to laboratory measurements. However, to date, none of these instruments have been operating continuously and reported any multiwavelength measurements of Saharan dust. The imaging technique is being expanded worldwide with further designs, although it is still limited to laboratory operation (Moallemi et al., 2023). All designs in polar nephelometry present physical limitations that limit the measurements to the range 3–178°, but synthetic tests have revealed that multiwavelength polarimetric PI-Neph measurements improve the information content for the retrieval of aerosol optical and microphysical properties (Moallemi et al., 2022). Therefore, measurements of dust phase matrix elements for ambient aerosol samples in the atmosphere will serve to advance in the understanding of mineral dust absorption properties and chemical composition (Di Biagio et al., 2017, 2019).

This work presents phase matrix measurements of ambient Saharan dust particles by the GRASP-Earth's (https://www.grasp-earth.com/, last access: 18 June 2025) multiwavelength PI-Neph. The instrument was developed using the heritage of previous PI-Neph developments conducted by UMBC and can provide aerosol phase matrix elements at 405, 515 and 660 nm of ambient samples in the range 5–175° with 1° resolution. Measurements were acquired in the urban background station (UGR) of the Andalusian Global ObseRvatory of the Atmosphere (AGORA) located in the southeast of the Iberian Peninsula, where the main source of natural particles is the Sahara's transported particles (Querol et al., 2019). We present the results for extreme outbreaks that occurred in March 2022 (Rodríguez and López-Darias, 2024) with PM_{10} (particulate matter with diameter $< 10\,\mu m$) concentrations over $1000\,\mu g m^{-3}$ and for more typical situations of moderate dust events with PM_{10} concentrations around $100\,\mu g\,m^{-3}$. The measurements presented of the phase matrix for Saharan dust are unique and are a step forward from the ancillary measurements performed in the region by Horvath et al. (2018) with single-wavelength polar nephelometry (no polarization was available).

This work is structured as follows: in Sect. 2 we describe the experimental station and the instrumentation, Sect. 3 gives an overview of the extreme dust events, Sect. 4 analyzes the results of the optical properties during different dust events, in Sect. 5 we discuss the results obtained, and Sect. 6 is devoted to the main conclusions and key points for future work.

2 Experimental station and instrumentation

2.1 Experimental station

Experimental measurements were carried out at the UGR station of AGORA in the city of Granada (37.18° N, 3.58° W; 680 m a.s.l.) in southern Spain. The main local source of aerosol particles at the UGR station is road traffic (Titos et al., 2014, 2017), with the sporadic presence of biomass burning aerosol (Casquero-Vera et al., 2021; Titos et al., 2017). Air-mass stagnation also favors the accumulation of pollution (Lyamani et al., 2012; Patrón et al., 2017). The city is located 200 km away from the African continent, so long-range transport of Saharan dust to the UGR station is quite common (Lyamani et al., 2010; Valenzuela et al., 2012a, b). These dust intrusions have mean aerosol optical depths (AODs) of 0.25 ± 0.12 (Pérez-Ramírez et al., 2016) and PM_{10} concentrations ranging between 25 and $200\,\mu g\,m^{-3}$ (Párraga et al., 2021), although extreme Saharan dust events with

AOD above 1.0 also affect the station (Guerrero-Rascado et al., 2009; Bazo et al., 2023). Most of these intrusions typically occur in summer, but in recent years they have become more frequent during the winter season (Cazorla et al., 2017; Cuevas-Agulló et al., 2024; Fernández et al., 2019; Titos et al., 2017).

In this study, particles were sampled using a total inlet (no size cut) that consists of a 5 m long stainless-steel tube with a 20 cm diameter (Lyamani et al., 2008). Inside the stainless-steel tube there are several pipes that split the aerosol flow into the different instruments. The inlet system is completely vertical to minimize deposition losses. The final connection to the instruments is performed with conductive tubing avoiding bends. Additionally, all the measurements were at ambient conditions (no aerosol dryer was used). Given the flow rate used in the measurements, we can assume that particles are randomly oriented, avoiding the limitations in polarization results of super-coarse particles with particle speed that can orient the particle in particular orientations (Daugeron et al., 2006).

2.2 Instrumentation

2.2.1 Polarized imaging nephelometer (PI-Neph)

The PI-Neph (GRASP-Earth PIN-100) is used to obtain direct measurements of two aerosol phase matrix elements, the phase function (F_{11}) and the polarized phase function ($-F_{12}/F_{11}$), at three different wavelengths (405, 515 and 660 nm). The instrument uses previous heritage in PI-Neph developments at the University of Maryland, Baltimore County (Dolgos and Martins, 2014), where the novelty in the PIN-100 is the use of one beam instead of a mirror system to fold the laser beam, as was in previous models. This feature minimizes internal reflection and loss of energy within the laser beam and guarantees that all points along the laser beam will have the same scattering plane orientation, assuring the optimal input polarization state at all scattering angles simultaneously. The optical system counts with a wire grid polarizer and two liquid-crystal variable retarders (LCVRs) that control the state of linear polarization. In this sense, polarized light (parallel or perpendicular) reaches the sample chamber. The light scattered by the aerosol particles is recorded with a 185° field-of-view CMOS camera, giving the scattered light by the particles in the sample chamber in the range 5–175°, with 1° angular resolution. More details of the instrument are in Bazo et al. (2024).

An extensive analysis of the error sources in the PI-Neph was performed in Bazo et al. (2024), but an overview is given here: an exhaustive calibration of the instrument is performed consisting of two different steps. The first is a geometric correction that corrects from the different light paths to the different pixels in the CMOS camera. Later, the absolute calibration permits us to obtain phase matrix elements in physical units. In each step we used known scatterers (CO_2 and particle-free air), whose parallel and perpendicular signals can be computed analytically using Rayleigh theory (Anderson et al., 1996). Evaluation of the calibration with time did reveal great stability (variations around 3 %). Instrument stability was evaluated with CO_2 measurements at a constant flow rate of 10 L min^{-1} during 15 min. These measurements revealed constant values of scattering coefficients with differences below 1 % versus theoretical values from Bodhaine et al. (1991). Finally, inherent aspects of the imaging technique were evaluated such as the impact of the exposure time. The largest noise is found for exposure times below 5 s, while the smoother values are obtained for exposure times of 10–20 s. However, large exposure times can yield more angles that are saturated, and the software must find a compromise between noise and saturation. Thus, the typical exposure time is 10 s, and with that we estimate that uncertainties in measured parallel and perpendicular signals are around 5 % in laboratory conditions. The evaluation of the instrument versus known scatterers (monodisperse polystyrene latex (PSL) spheres) showed good agreement, the RMSE being around 0.10 for both F_{11} and $-F_{12}/F_{11}$.

The uncertainties in direct measurements of the instrument (parallel and perpendicular signals) are 5 %, which implies uncertainties below 10 % in F_{11} and below 20 % in $-F_{12}/F_{11}$. However, in situ measurements present natural variability of the aerosol sampled, and the differences could be enhanced because of the short exposure times ($\sim$ 10 s). Effects during the measurements such as saturation or low signal-to-noise ratios (SNRs) of some pixels can happen. Other issues such as the passage of an individual super-coarse particle can have an impact on certain angles of the phase matrix. Therefore, we apply a data quality check procedure that accounts for all these issues and provide an effective phase matrix representative of an average time of 30 min or 1 h, depending on the specific conditions of natural aerosol variability. Note that standard deviations during these periods might be larger than the uncertainties of the instrument. Details of this quality check procedure are in Bazo et al. (2024).

The direct measurements of F_{11} and $-F_{12}/F_{11}$ with the PI-Neph allow us to obtain other aerosol optical parameters such as the scattering coefficient (σ), the asymmetry parameter (g) and the fraction of backscattered light (B_s) using the following equations (Horvath et al., 2018):

$$\sigma_{sca}(\lambda) = \frac{1}{2}\int_0^{180} F_{11}(\theta,\lambda)\sin\theta \cdot \mathrm{d}\theta, \tag{1}$$

$$P_{11}(\theta,\lambda) = \frac{F_{11}(\theta,\lambda)}{\sigma_{sca}(\lambda)}, \tag{2}$$

$$g(\lambda) = \int_0^{\pi} P_{11}(\theta,\lambda)\cdot\sin\theta\cdot\cos\theta\cdot\mathrm{d}\theta, \tag{3}$$

$$B_s(\lambda) = \frac{1}{2}\int_{\frac{\pi}{2}}^{\pi} P_{11}(\theta,\lambda)\cdot\sin\theta\cdot d\theta, \tag{4}$$

where data from 0 to 5° and from 175 to 180° have been linearly extrapolated to obtain the complete phase function.

Stepwise extrapolations might be more consistent (i.e., Horvath, 2015), but our additional computations remarked that differences between linear and stepwise extrapolations were below 1 % for σ_{sca}, g and B_{s}. For particle sizes above 4 µm the uncertainties can yield 5 % (Horvath, 2015).

2.2.2 Additional in situ instrumentation at AGORA

AGORA operates other in situ instruments within the Aerosols, Clouds and Trace Gases Research Infrastructure (ACTRIS; https://www.actris.eu/, last access: 18 June 2025). The integrating nephelometer (TSI model 3563) was used to measure the aerosol particle light scattering coefficient (σ_{sca}) at 450, 550 and 700 nm with a flow rate of $15\,\mathrm{L\,min^{-1}}$ and a time resolution of 1 min. As with the PI-Neph, the integrating nephelometer is calibrated with particle-free air and CO_2, and Rayleigh subtraction is applied to measure particle scattering only. Due to experimental limitations the scattered light in the complete forward (0°) and backward (180°) regions cannot be detected, so the angular range for integration is 7–170°. However, results used in this work have been corrected to the entire angular range with the correction proposed by Anderson and Ogren (1998). On the other hand, we also used the multiwavelength aethalometer (AE33, Magee Scientific) that measures the aerosol light absorption coefficient (σ_{abs}) at seven different wavelengths (370, 470, 520, 590, 660, 880 and 950 nm) with a flow rate of $4\,\mathrm{L\,min^{-1}}$ and a time resolution of 1 min. Equivalent black carbon (eBC) concentration is inferred by measuring the absorption coefficient at 880 nm using a mass absorption cross section of $7.77\,\mathrm{m^2\,g^{-1}}$ (Titos et al., 2017). Measurements of the absorption coefficient by the aethalometer are corrected with the one measured by the Multiangle Absorption Photometer (MAAP; model 5012, Thermo Fisher) at 637 nm. More details of the instruments are in Drinovec et al. (2015) and Petzold and Schönlinner (2004), respectively.

The scattering and absorption coefficients measured by the integrating nephelometer and the aethalometer, respectively, have been used to calculate the scattering Ångström exponent (SAE) and the absorption Ångström exponent (AAE):

$$\mathrm{SAE}_{\lambda_1-\lambda_2} = -\frac{\ln\left(\frac{\sigma_{\mathrm{sca}}(\lambda_1)}{\sigma_{\mathrm{sca}}(\lambda_2)}\right)}{\ln\left(\frac{\lambda_1}{\lambda_2}\right)}, \tag{5}$$

$$\mathrm{AAE}_{\lambda_1-\lambda_2} = -\frac{\ln\left(\frac{\sigma_{\mathrm{abs}}(\lambda_1)}{\sigma_{\mathrm{abs}}(\lambda_2)}\right)}{\ln\left(\frac{\lambda_1}{\lambda_2}\right)}. \tag{6}$$

The wavelengths used in this work to calculate both SAE and AAE were 405–660 and 450–700 nm, respectively. Moreover, measurements of σ_{abs} combined with those of σ_{sca} permit the computation of the extinction coefficient $\sigma_{\mathrm{ext}} = \sigma_{\mathrm{abs}} + \sigma_{\mathrm{sca}}$, thus obtaining aerosol single scattering albedo (SSA) as

$$\mathrm{SSA} = \frac{\sigma_{\mathrm{sca}}}{\sigma_{\mathrm{ext}}}, \tag{7}$$

where the Ångström law is used to calculate σ_{abs} for the PI-Neph wavelengths. On the other hand, if $F_{11}(180°)$ is computed the extinction-to-backscattering ratio, widely known as lidar ratio (LRs) in the lidar community, can be computed as

$$\mathrm{LR} = \frac{\sigma_{\mathrm{ext}}}{F_{11}(180°)}. \tag{8}$$

The computation of $F_{11}(180°)$ has been done using the interpolation method used for completing the entire angular range in σ_{sca}. Other more robust methods can be used (i.e., Gómez Martín et al., 2021) that can imply differences in $F_{11}(180°)$ of up to 20 %–30 %. Therefore, LR estimations will serve as an illustration of how this parameter varies under different conditions. We highlight that PI-Neph is not designed to accurately measure $F_{11}(180°)$, and there are other specific instruments that serve that purpose (Järvinen et al., 2016; Miffre et al., 2023; Sakai et al., 2010).

3 Overview of extreme dust events during March 2022

During March 2022 the Iberian Peninsula, and particularly its southeast region, was affected by two intense Saharan dust outbreaks, especially during 15–16 and the 24–25 March. Figure 1 shows the geopotential height maps at 850 mb for 15 March 18:00 UTC and 25 March 12:00 UTC, which are close to the peaks of the event in each case. Data shown are from the NCEP/NCAR model (Kalnay et al., 1996; Kanamitsu et al., 2002) – https://tropic.ssec.wisc.edu/archive, last access: 11 June 2025). On 15 March, Fig. 1a indicates the low-pressure system centered in the southwest of the Iberian Peninsula and northern Morocco, associated with low values of geopotential heights. A high-pressure system is present in the central Mediterranean, associated with high values of geopotential height. This high-pressure system covers wide regions from central Europe to the Sahara in Libya and Tunisia. The interaction between these low-pressure and high-pressure systems favors strong southeastern winds to the south of the Iberian Peninsula. On 25 March, Fig. 1 reveals very similar patterns, although the low-pressure system is less intense (more sparse lines) and is displaced a little bit towards the east, centered over northern Morocco.

The synoptic situations on 15 and 25 March described in Fig. 1 implied the advection of hot and dry air from the Sahara region in Algeria and southern Morocco. The low-pressure system favored wind gusts and thus the injection of dust particles in the atmosphere, which are later transported long distances by the low-pressure system. This is one of the classical transport patterns of Saharan dust to the Iberian Peninsula (Escudero et al., 2005; Rodríguez et al., 2001; Salvador et al., 2014).

Figures 2 and 3 show total aerosol optical depth (AOD) at 550 nm generated by the CAMS model (Benedetti et al., 2009; Morcrette et al., 2009) over Europe. The wind field at the surface is also represented in these figures, and different times selected serve to understand how the dust was transported and how it affected different regions. Figure 2 clearly shows the counterclockwise winds associated with the low-pressure system and how this hot and dry air enters through the southeast reaching the north of the Iberian Peninsula and southern France. That air mass also transports large amounts of mineral dust particles, as can be observed by the high values of simulated AODs. It is observed that the largest intensity of dust particles in the southeast of the Iberian Peninsula happened on the evening of 15 March. The wind pattern reveals how dust enters through the southeast of the Iberian Peninsula, later reaching the northwest latitudes. The weak wind pattern in the north of the Iberian Peninsula favors the transport to southern France. For 25 March (Fig. 3), the wind pattern is very similar to that on 15 March (Fig. 2), although it does not reach the same northern locations. Indeed, the low-level system configuration seems to facilitate the transport of this hot and dry air to western locations in Portugal and the Atlantic Ocean. The CAMS model also predicts a larger amount of dust particles as indicated by the high AODs.

Figure 4 shows satellite images provided by NASA Worldview (https://wvs.earthdata.nasa.gov) that allow us to have a visualization of the intensity of the dust outbreaks over the Iberian Peninsula. On both days, there were clouds in the Iberian Peninsula because of the advection of humidity from the Atlantic by the low-pressure system (more intense on 25 March, which explains that almost all the Iberian Peninsula was covered by clouds). The image for 15 March clearly shows the high presence of dust in the north of the Iberian Peninsula, the Cantabrian Sea and southern France. For 25 March the cloud cover hinders dust visualization, but it is observed in the Atlantic in the region between the Canary and Madeira islands. We highlight the fact that such extreme events are not typical in the winter season in the Iberian Peninsula, although it is not the first time that similar dust events have been recorded in this season (Cazorla et al., 2017; Fernández et al., 2019; Titos et al., 2017).

The events on 15 and 25 March 2022 can be considered extreme Saharan dust outbreaks because of the large area covered but especially because of the large number of mineral dust particles transported. A more in-depth analysis of satellite images revealed that for the cloud-free pixel, recorded AODs were between 1.9–2.5 on 15 March and between 0.3–1.5 on 25 March, which are very high for these locations. The extremely high AOD values on 15 March associated with dust particles were confirmed by AERONET observations, with AODs above 1.0 for the stations in northern Spain (A Coruña and Palencia) and southern France (Aubiere, Agen, Archaon and Momuy), where data of Level 2.0 Version 3 are available – graphs are not shown for clarity but can be visualized on the AERONET web page (https://aeronet.gsfc.nasa.gov/, last access: 21 February 2023). These high values of AODs agree with those reported by the CAMS model in Figs. 2 and 3. Unfortunately, there are no AERONET Level 2.0 Version 3.0 data available on 25 March due to cloud coverage in the AERONET stations. For both events, the urban background air-quality surface station in Granada (Palacio de Congresos (PAL) https://www.juntadeandalucia.es/medioambiente/portal/home, last access: 18 January 2023) recorded 10 min PM_{10} concentrations, which were up to $2500\,\mu g\,m^{-3}$ on 15 March and up to $800\,\mu g\,m^{-3}$ on 25 March, values that are way above the usual PM_{10} values ($\sim 100\,\mu g\,m^{-3}$) recorded at Granada during usual dust outbreaks (Párraga et al., 2021). On this day, lidar measurements in AGORA in the framework of the European Aerosol Research Lidar Network (EARLINET; https://www.earlinet.org/, last access: 14 October 2024) were saturated in the first 1–2 km and prevented any kind of retrieval of aerosol optical properties. Nevertheless, these measurements served to illustrate that most of the transport occurred in the first 2 km above the ground.

4 Results of aerosol phase matrix from different dust scenarios

4.1 Extreme events

For the two extreme events recorded on 15 and 25 March 2022, Fig. 5 shows hourly averages of different aerosol properties obtained by the in situ instruments at UGR station. In particular, we show eBC concentrations measured by the AE33; $\sigma_{sca}(\lambda)$ measured by the PI-Neph; and SAE, AAE (both calculated between 405 and 660 nm), $g(\lambda)$, $B_s(\lambda)$, SSA(λ) and LR(λ) derived from measurements of both instruments. PM_{10} concentrations are also shown, which were obtained from the PAL air-quality station ($\sim$600 m distance from UGR station). Panel (a) in Fig. 5 shows the results for the event on 15–16 March, while panel (b) is for the event on 24– 25 March. Note that panel (a) in Fig. 5 does not cover the beginning of the Saharan dust event due to lack of data related to supersaturation of the PI-Neph's measurements.

For the event on 15–16 March, Fig. 5a.1 reveals extremely high PM_{10} with an average of $794\,\mu g\,m^{-3}$, which is over the regulatory daily limit value of $50\,\mu g\,m^{-3}$ established by the Ambient Air Quality Directive (European Union, 2008). Maximum values of hourly PM_{10} concentrations are recorded at around 16:00 UTC, with values up to $18:00\,\mu g\,m^{-3}$ approximately. The scattering coefficient time series shows the same behavior as the PM_{10}, with maximum values of σ_{sca} at the same time as the peak of the PM_{10} concentration. The mean value ($\pm$SD) of SAE is 0.01 ± 0.15, which increases to 0.20 when PM_{10} concentrations reach their maximum. Such values of SAE suggest clear predominance of large particles. For the g parameter (Fig. 5a.4) ap-

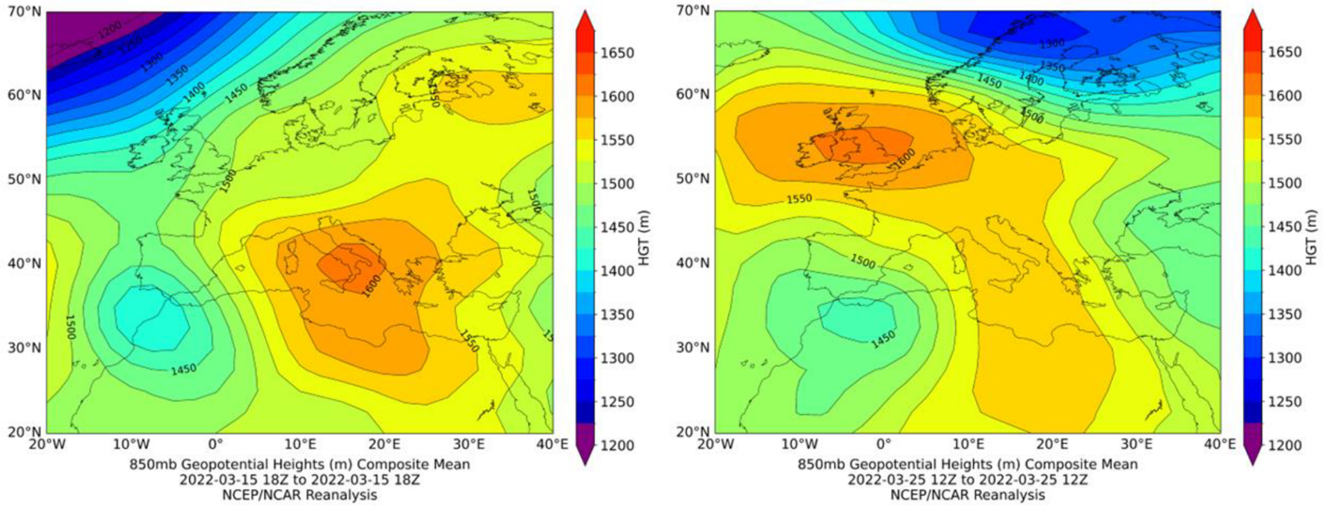

Figure 1. Geopotential height at 850 mb for **(a)** 15 March 2022 at 18:00 UTC and **(b)** 25 March 2022 at 12:00 UTC. Data are from NCEP/NCAR – https://tropic.ssec.wisc.edu/archive (last access: 14 October 2024).

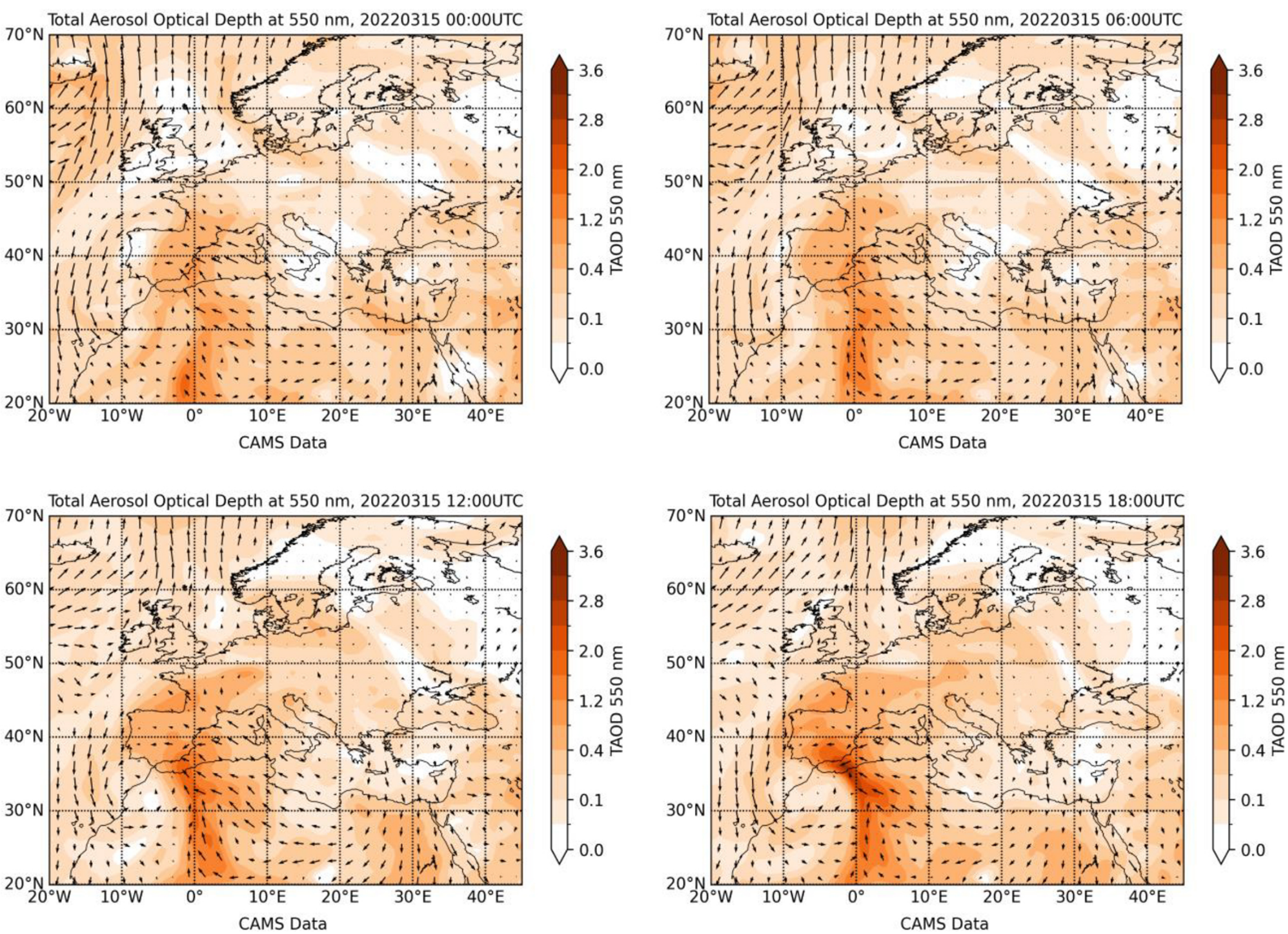

Figure 2. CAMS model simulations of total aerosol optical depth (TAOD) and wind field for different times on 15 March 2022.

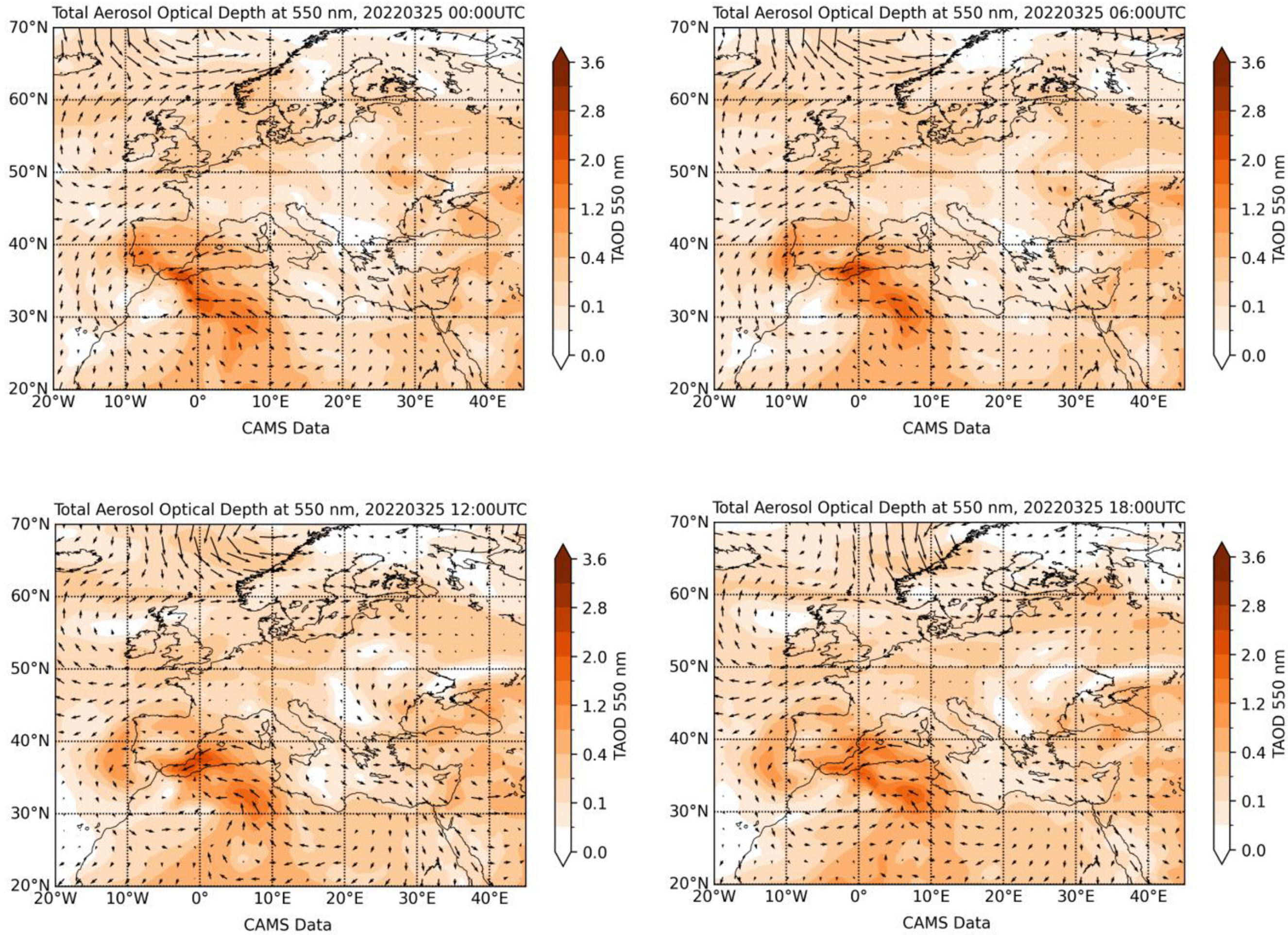

Figure 3. CAMS model simulations of total aerosol optical depth (TAOD) and wind field for different times on 25 March 2022.

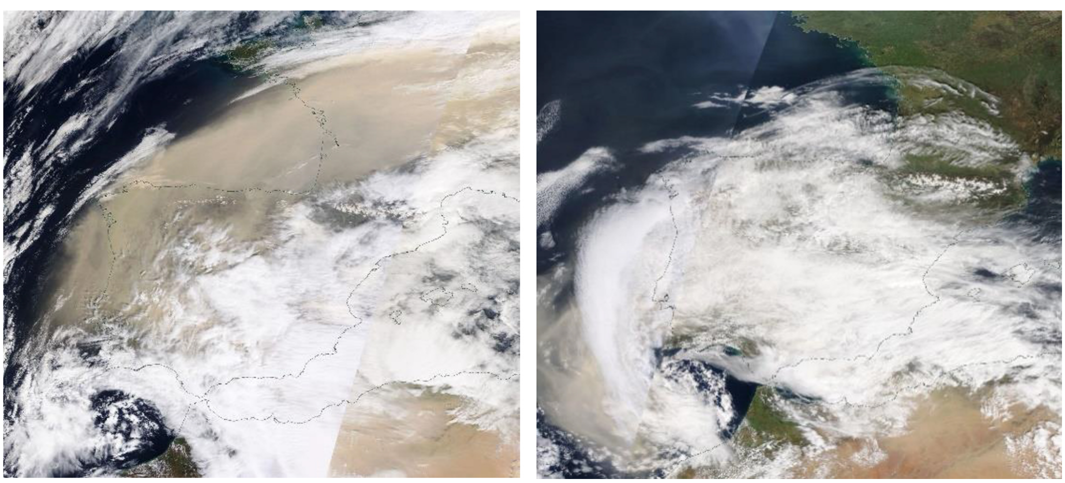

Figure 4. (a) Satellite image from 15 March 2022. **(b)** Satellite image from 25 March 2022. Images from https://wvs.earthdata.nasa.gov (last access: 21 February 2023), obtained with MODIS (Moderate Resolution Imaging Spectroradiometer).

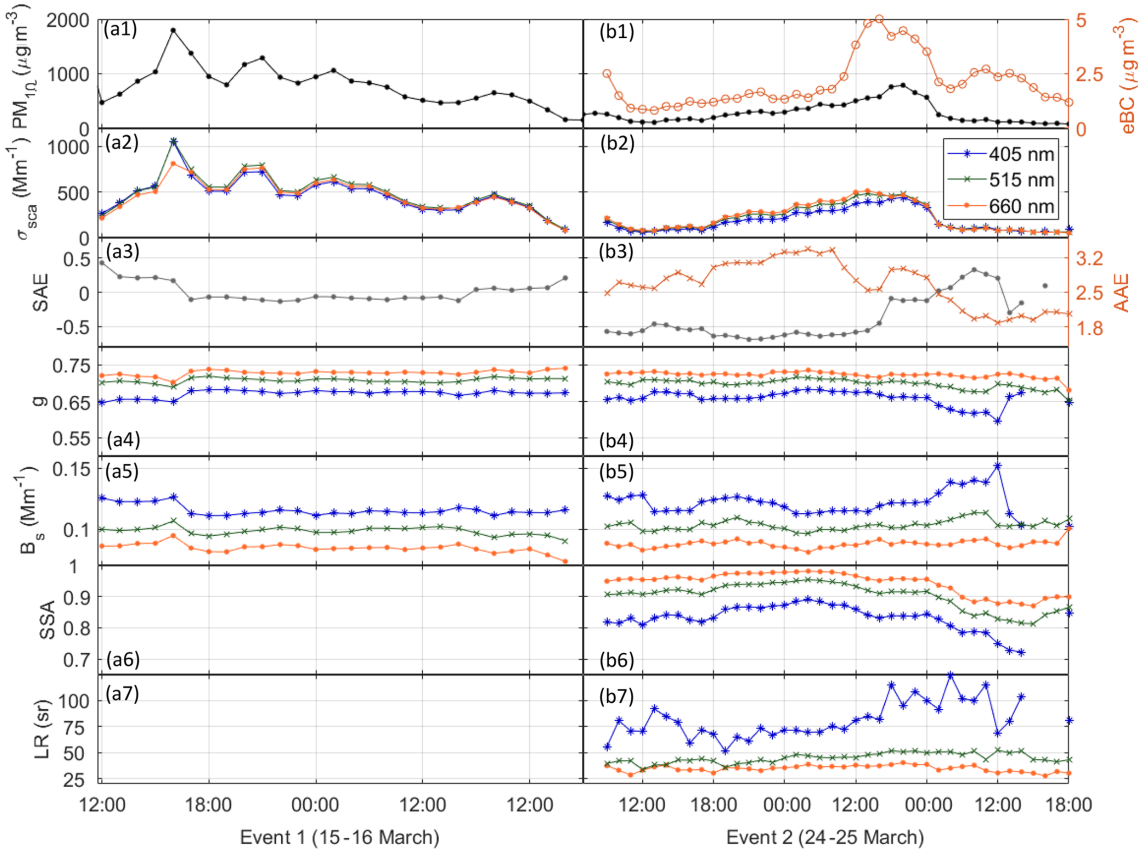

Figure 5. Time series of the PM_{10} and eBC concentrations (**a**.1, **b**.1), σ_{sca} (scattering coefficient) (**a**.2, **b**.2), SAE (scattering Angström exponent) and AAE (absorption Angström exponent) (**a**.3, **b**.3), g (asymmetry parameter) (**a**.4, **b**.4), B_s (fraction of backscattered light) (**a**.5, **b**.5), SSA (single scattering albedo) (**a**.6, **b**.6), and LR (lidar ratio) (**a**.7, **b**.7) for the extreme dust events of 15 March **(a)** and 24 March 2022 **(b)**.

proximately constant values are observed with mean values of 0.672 ± 0.010, 0.701 ± 0.006 and 0.729 ± 0.007 for 405, 515 and 660 nm, respectively, which are typical values for transported dust particles (Horvath et al., 2018). Also, Horvath et al. (2018) found an averaged B_s of 0.094 at 532 nm for Saharan dust, which agrees with the results shown in Fig. 5a.5 for the 515 nm wavelength (0.098 ± 0.003). The low values of the B_s observed at the three wavelengths are associated with small values of F_{11} at the backward scattering angles, which is common for non-spherical particles (Horvath et al., 2018). The lack of aethalometer data did not allow eBC, AAE, SSA and LR analyses for this day.

For the event on 24–25 March, the average PM_{10} concentration is $283\,\mu g\,m^{-3}$. These PM_{10} concentrations (Fig. 5b.1) increase until 10:00 UTC, when the maximum hourly value of $790\,\mu g\,m^{-3}$ is reached. These values are lower than those recorded on 15 March, but again they are very high and above the daily limit of the European Directive. Scattering coefficients at the time of PM_{10} concentration peak are 468, 476 and $441\,Mm^{-1}$ for the 660, 515 and 405 nm wavelengths, respectively. After this peak, both PM_{10} and σ_{sca} decrease, suggesting the end of the extreme dust outbreak. The SAE main feature is its approximately constant value of -0.5 until early in the morning on 25 March, when it starts to slightly increase. This pattern suggests clear predominance of large particles during the dust outbreak, while the increase in the morning can be associated with additional influence of small particles, likely originated from road traffic during morning traffic rush hour (Lyamani et al., 2010). On the other hand, the AAE shows a different behavior, with high values at the beginning of the time series, representative of mineral dust, and a later decrease to values around 1.7, coincident with the decrease in PM_{10}. These values of AAE are in the range of those reported by Valenzuela et al. (2015) for a mixture of dust and black carbon particles and also agree with the patterns of eBC and PM_{10} that suggest a larger contribution of eBC to the total PM_{10} concentration at the end of the dust event than at the peak. On the other hand, g mean values are 0.659 ± 0.020, 0.698 ± 0.013 and 0.723 ± 0.009 for 405, 515 and 660 nm, respectively, very similar to those observed for the other extreme event on 15–16 March. For the B_s, (Fig. 5.5) a similar behavior to the previous event is observed again (Fig. 5a.5), with values around 0.1 for the 515 nm wavelength and below 0.15 in the three channels. The channel at 405 nm seems to be the most sensitive in g and B_s to changes in dust concentration since the time when a sharp change happens (25 March at 14:00 UTC) coincides with the hour when PM_{10} decreases and eBC increases, indicating more contribution of eBC to the total ensemble of particles.

Aethalometer measurements during 24–25 March allowed the study of further aerosol optical properties: the SSA (Fig. 5b) shows the highest values for all three wavelengths during the dust outbreaks. However, there is a strong spectral dependency, since the SSA at 405 nm clearly shows lower values (~ 0.85) compared to the other wavelengths that present SSA above 0.9. As the PM_{10} concentration decreases (and eBC concentration contribution to the mixture increases), the SSA shows smaller values with a stronger decrease in the 405 nm wavelength. Lastly, Fig. 5b.7 shows the time series of the LR during the second dust event, on 25 March. The LRs at 515 and 660 nm are rather constant, with mean values of 45 ± 5 and 35 ± 3 sr, respectively. However, the LR at 405 nm shows higher values and variability, with 81 ± 18 sr. The LR at 515 nm is very similar to the values measured by lidar systems at 532 nm for transported Saharan dust layers (Groß et al., 2013). Thus, the hypothesis that after 14:00 UTC the presence of pollution particles becomes more relevant implies a decrease in SSA and illustrates variability in LRs, particularly at 405 nm.

Phase matrix elements were exhaustively monitored with the use of the PI-Neph during both extreme events. Given the high concentrations of large particles, the usual configuration of the measurements could lead to saturation of many angles in the forward scattering. Therefore, it was necessary to reduce the gain of the PI-Neph's camera, changing the dynamic range of the camera for obtaining non-saturated measurements at such high concentrations. But these changes were made to also guarantee enough signals in the backward region where the minimums are found. Nevertheless, sporadic pixels might present saturation or low SNR at some angles, but they were filtered out by the data quality criterion for the instrument (Sect. 2.2.1). For the specific phase function measurements where many data points are rejected, all angles are eliminated because phase matrix measurements were considered non-reliable. Moreover, $-F_{12}/F_{11}$ is computed by subtracting first parallel and perpendicular phase functions that in many angles are very similar. Dividing this small number by F_{11} can enhance the differences, which is particularly critical in the angular regions where the minimum values of scattering are found (typically between 90–150° for dust particles). All these effects, although they are always present, imply larger random noise in the measurements. Actually, noisier patterns in measured F_{11} and $-F_{12}/F_{11}$ affected by large particles when compared with measurements of anthropogenic origin have already been reported by the first versions of PI-Neph in the United States (Espinosa et al., 2018).

Figure 6 shows F_{11} and $-F_{12}/F_{11}$ phase matrix elements for the event on 15–16 March 2022 at four different representative stages. Data are 60 min averages, where the standard deviations represent the variability of the different parcels of air sampled throughout the hour of measurements. These standard deviations are around 20 % of the average values for F_{11} and range between 0.1 and 0.2 for $-F_{12}/F_{11}$. Note that the large standard deviation can be explained by the specific issues for the measurements of dust particles commented above. Detailed hourly evolutions can be found in the Supplement (Figs. S1–S2). Mean hourly averages of intensive and extensive aerosol parameters for the time periods shown in Fig. 6 are given in Table 1, particularly PM_{10}, σ_{sca}, SAE, AAE and g – note that SSA and LR were not available due to the lack of aethalometer data for that day. Error bars in Table 1 are the standard deviations of the hourly mean values. Just before the impact of the extreme dust plume on 15 March 07:00 UTC (Fig. 6a), values of PM_{10} ($\sim 61\,\mu g\,m^{-3}$) and SAE (~ 1.65) can be considered to be the background in the station and represent a mixture between fine- and coarse-mode particles. Later, on 15 March at 12:00 UTC (Fig. 6b), the drastic increase in PM_{10} ($\sim 473\,\mu g\,m^{-3}$) and decrease in SAE (~ 0.43) highlight a much larger contribution of coarse-mode particles. Extreme values of PM_{10} of $\sim 1375\,\mu g\,m^{-3}$ on 15 March at 17:00 UTC (Fig. 6c) corresponds to the peak of the event. The lowest SAE (-0.11) was recorded at that moment, and therefore a large contribution of coarse particles is expected. Finally, on 16 March at 13:00 UTC (Fig. 6d), the decrease in PM_{10} ($\sim 338\,\mu g\,m^{-3}$) and the increase in SAE (~ 0.07) seem to indicate that the Saharan dust plume starts to withdraw.

Figure 6 shows a general pattern in F_{11} characterized by strong predominance of forward scattering up to 2 orders of magnitude greater than backward scattering. However, there are significant changes in both magnitudes and spectral dependence over time, that is, with the intensity of the dust outbreak passage. At the beginning of the dust event (Fig. 6a), the values of F_{11} in the forward scattering region are around $1000\,Mm^{-1}\,sr^{-1}$ for all three wavelengths, which is even 1 order of magnitude lower when compared with the cases at the other moments of the event (i.e., $50\,000\,Mm^{-1}\,sr^{-1}$ for the three channels during the peak). Also, at the beginning of the event (Fig. 6a), notable spectral separation in F_{11} is observed, while such spectral separation is negligible during the rest of the event when coarse-mode particles largely predominate. All F_{11} values show the minimum in the region 120–140°, but the magnitude of that minimum varies between the different stages. Also, around that minimum is the region where some spectral difference is observed during the cases of strong predominance of the coarse mode (Fig. 6c–d). A recovery from that minimum is also observed, being more pronounced in cases close to the peak of the event.

Figure 6 shows that the differences in $-F_{12}/F_{11}$ patterns and wavelengths dependences with time are more remarkable than those observed for F_{11}. At the beginning $-F_{12}/F_{11}$

Table 1. Hourly averaged properties of different stages of the extreme dust outbreaks in March 2022 reported in Figs. 6 and 7. The properties are reported at three wavelengths in the order of 660, 515 and 405 nm from top to bottom. Only the angular range of the PI-Neph (5–175°) is used as the integration range of σ_{sca}. Error bars correspond to the standard deviations of the hourly means.

	PM_{10} ($\mu g\,m^{-3}$)	eBC ($\mu g\,m^{-3}$)	σ_{sca} (Mm^{-1})	SAE	AAE	g	B_s (Mm^{-1})	SSA	LR (sr)
15 Mar 07:00	61 ± 5	–	55 ± 3 84 ± 4 123 ± 7	1.65 ± 0.13	–	0.573 ± 0.015 0.604 ± 0.018 0.616 ± 0.008	0.135 ± 0.013 0.117 ± 0.011 0.116 ± 0.004	–	–
15 Mar 12:00	473 ± 131	–	215 ± 36 241 ± 38 265 ± 39	0.43 ± 0.13	–	0.722 ± 0.001 0.703 ± 0.001 0.641 ± 0.001	0.086 ± 0.005 0.100 ± 0.007 0.126 ± 0.005	–	–
15 Mar 17:00	1376 ± 256	–	718 ± 128 746 ± 112 682 ± 101	-0.11 ± 0.12	–	0.734 ± 0.008 0.715 ± 0.009 0.679 ± 0.009	0.084 ± 0.005 0.096 ± 0.005 0.113 ± 0.006	–	–
16 Mar 13:00	338 ± 48	–	178 ± 47 191 ± 52 184 ± 50	0.07 ± 0.13	–	0.739 ± 0.008 0.713 ± 0.008 0.673 ± 0.011	0.079 ± 0.005 0.095 ± 0.005 0.113 ± 0.006	–	–
24 Mar 13:00	108 ± 14	0.81 ± 0.10	76 ± 13 70 ± 12 65 ± 8	-0.46 ± 0.22	2.58 ± 0.10	0.733 ± 0.024 0.709 ± 0.031 0.664 ± 0.035	0.084 ± 0.014 0.098 ± 0.020 0.117 ± 0.018	0.955 ± 0.004 0.912 ± 0.006 0.832 ± 0.006	36 ± 10 38 ± 11 92 ± 20
24 Mar 21:00	297 ± 21	1.59 ± 0.14	284 ± 27 257 ± 25 205 ± 16	-0.69 ± 0.18	3.09 ± 0.03	0.725 ± 0.025 0.701 ± 0.025 0.659 ± 0.021	0.088 ± 0.016 0.105 ± 0.017 0.124 ± 0.015	0.975 ± 0.001 0.940 ± 0.001 0.867 ± 0.003	34 ± 4 40 ± 6 61 ± 16
25 Mar 09:00	760 ± 44	4.21 ± 0.21	466 ± 15 461 ± 17 427 ± 14	-0.09 ± 0.06	2.96 ± 0.05	0.725 ± 0.007 0.705 ± 0.009 0.662 ± 0.007	0.087 ± 0.005 0.101 ± 0.006 0.122 ± 0.005	0.957 ± 0.002 0.915 ± 0.003 0.838 ± 0.005	39 ± 5 52 ± 6 115 ± 8
25 Mar 20:00	116 ± 6	2.3 ± 0.5	80 ± 7 78 ± 6 74 ± 3	-0.16 ± 0.18	2.03 ± 0.08	0.722 ± 0.019 0.689 ± 0.020 0.667 ± 0.021	0.086 ± 0.011 0.104 ± 0.014 0.113 ± 0.011	0.876 ± 0.015 0.815 ± 0.020 0.722 ± 0.021	32 ± 7 52 ± 18 104 ± 10

shows very different spectral patterns with remarkable spectral separation: for 515 and 660 nm, $-F_{12}/F_{11}$ follows bell-shaped patterns with values near to zero at the edges (0 and 180°) and a maximum around 90° of 0.4 and 0.5 for 515 and 660 nm, respectively. However, for 405 nm, the pattern is markedly different, with maximum values of 0.1 occurring at around 80°, followed by a sharp decrease, reaching negative values of −0.4 close to 150°. For the two following cases (Fig. 6b.2 and 6c.2), which are close to the peaks of maximum intensity in the Saharan dust outbreak, $-F_{12}/F_{11}$ shows a distinct pattern characterized by almost negligible differences with wavelength and a very small bell-shaped pattern with maxima around 0.1 at ∼ 90°. Later, after the strong dust passage, for $-F_{12}/F_{11}$, Fig. 6d.2 shows a similar bell-shaped pattern at 515 and 660 nm, but there is presence of some negative values at 405 nm.

For the event on 24–25 March, Fig. 7 shows F_{11} and $-F_{12}/F_{11}$ phase matrix elements for four different representative instants during the event. The data correspond again to 60 min averages, with detailed hourly evolutions shown in the Supplement (Figs. S3–S4), where the standard deviations represent the variability of the samples. These standard deviations are around 20 % of the average values for F_{11} and around 0.2 for $-F_{12}/F_{11}$, showing larger variability during this dust event than in the previous one. Again, the specific issues related to the measurements of large particles can explain the deviations. Nevertheless, the larger deviations when compared with the previous events make us think that during this event there was more aerosol variability, which is critical for the regions of the minima in scattering. Mean hourly averages for these periods of intensive and extensive aerosol variables are again shown in Table 1, but now aethalometer measurements permit us to add eBC, SSA and LR. Once again, this event exhibits lower values in particulate matter and appears to be less intense when compared to the event on 15–16 March. However, it can still be considered an extreme event because the maximum PM_{10} concentrations (> 700 $\mu g\,m^{-3}$) recorded are above the typical values (∼ 100 $\mu g\,m^{-3}$) of Saharan dust transport to the UGR station (Párraga et al., 2021). Table 1 results serve to understand the temporal evolution of the extreme Saharan dust outbreak. On 24 March at 13:00 UTC the lowest PM_{10} (∼ 108 $\mu g\,m^{-3}$) values are recorded and can be associated with the background conditions before the intense outbreak. On 24 March 21:00 UTC the PM_{10} values (∼ 297 $\mu g\,m^{-3}$) are almost 3 times those recorded at noon and are associated with the entrance of the extreme event, while on 25 March at 09:00 UTC the largest PM_{10} values (∼ 796 $\mu g\,m^{-3}$) are

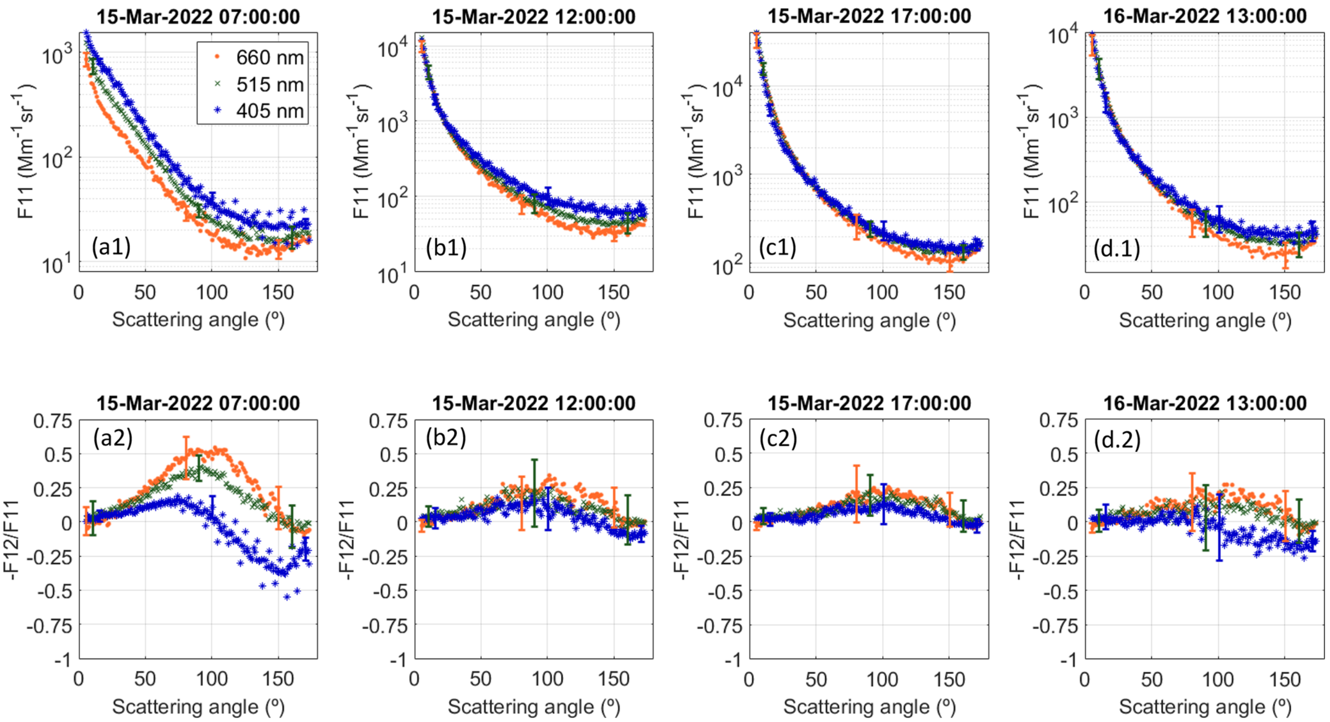

Figure 6. Hourly averages of phase function (F_{11}) and polarized phase function ($-F_{12}/F_{11}$) on 15–16 March 2022 for four different stages of the evolution of the extreme Saharan dust outbreak: **(a)** 15 March at 07:00 UTC before the Saharan dust outbreak reached the station, **(b)** 15 March at 12:00 UTC when the Saharan dust begins to reach the station, **(c)** 15 March at 17:00 UTC associated with the peak of the extreme Saharan dust intrusion, and **(d)** 16 March at 13:00 UTC when Saharan dust starts to withdrawn. Error bars correspond to the standard deviation of the hourly averages.

recorded, and that moment is associated with the peak of the event. Finally, on 25 March at 20:00 UTC the lowest values of PM_{10} are recorded ($\sim 116\,\mu g\,m^{-3}$), and that moment is associated with the withdrawal of the extreme event. For the cases of very high PM_{10} ($> 300\,\mu g\,m^{-3}$), although they present the largest eBC, the values of SAE and AAE suggest the large predominance of coarse-mode particles. But for the rest of the cases the mixture seems more complicated, and no conclusive claim can be made initially about the predominance of any kind of particles.

Figure 7 shows that F_{11} patterns are very similar to the previous extreme event on 15–16 March, with strong predominance of forward scattering ($\sim 25\,000\,Mm^{-1}\,sr^{-1}$), being 2 orders of magnitude above the backscattering ($\sim 100\,Mm^{-1}\,sr^{-1}$) at the peak of the event on 25 March 09:00 UTC. There are no significant spectral differences, as also happened for the other extreme event on 15–16 March. These patterns in F_{11} agree with laboratory measurements of dust samples (i.e., Muñoz et al., 2007; Renard et al., 2014; Volten et al., 2001). Nevertheless, there are some features in F_{11} with different situations: the slope in F_{11} in the forward scattering region becomes sharper when the PM_{10} concentrations are higher (Fig. 7b.1 and 7c.1). For the backward region F_{11} shows a flatter behavior for high PM_{10} concentrations (Fig. 7b.1 and c.1), while for the cases with lower PM_{10} concentrations there is a sharp increase in scattering from 150 to 180°. During the previous extreme dust outbreak, we observed flat patterns for the backward scattering region during the peaks of the dust intrusions.

Measurements of $-F_{12}/F_{11}$ in Fig. 7 exhibit several behaviors throughout the event. During the peaks of the event on 24–25 March (Fig. 7b–c), $-F_{12}/F_{11}$ patterns show minimal differences with wavelength and a very small bell-shaped pattern with maxima around 0.1 at 100°. However, there are differences when compared to the instants before the arrival of the dust outbreak (Fig. 7a) and when the dust is withdrawn (Fig. 7d). In these two cases $-F_{12}/F_{11}$ shows bell-shaped patterns for 515 and 660 nm, with maxima of approximately 0.2 around 100° and values close to zero in the regions for scattering angles below 50° and above 150°. These patterns in $-F_{12}/F_{11}$ agree with the observed for the other instants of the event. However, the pattern for 405 nm is markedly different from the rest, and it is characterized by almost flat values close to zero of $-F_{12}/F_{11}$ in the range of approximately 0–50°, followed by a sharp decrease reaching negative values of −0.6 close to 130°. Then, there is a sharp increase in $-F_{12}/F_{11}$, reaching values close to zero at 180°. Therefore, $-F_{12}/F_{11}$ at 405 nm appears to be highly sensitive to the possible influence of other particles in the mixture. It is also noteworthy that the maximum in eBC co-

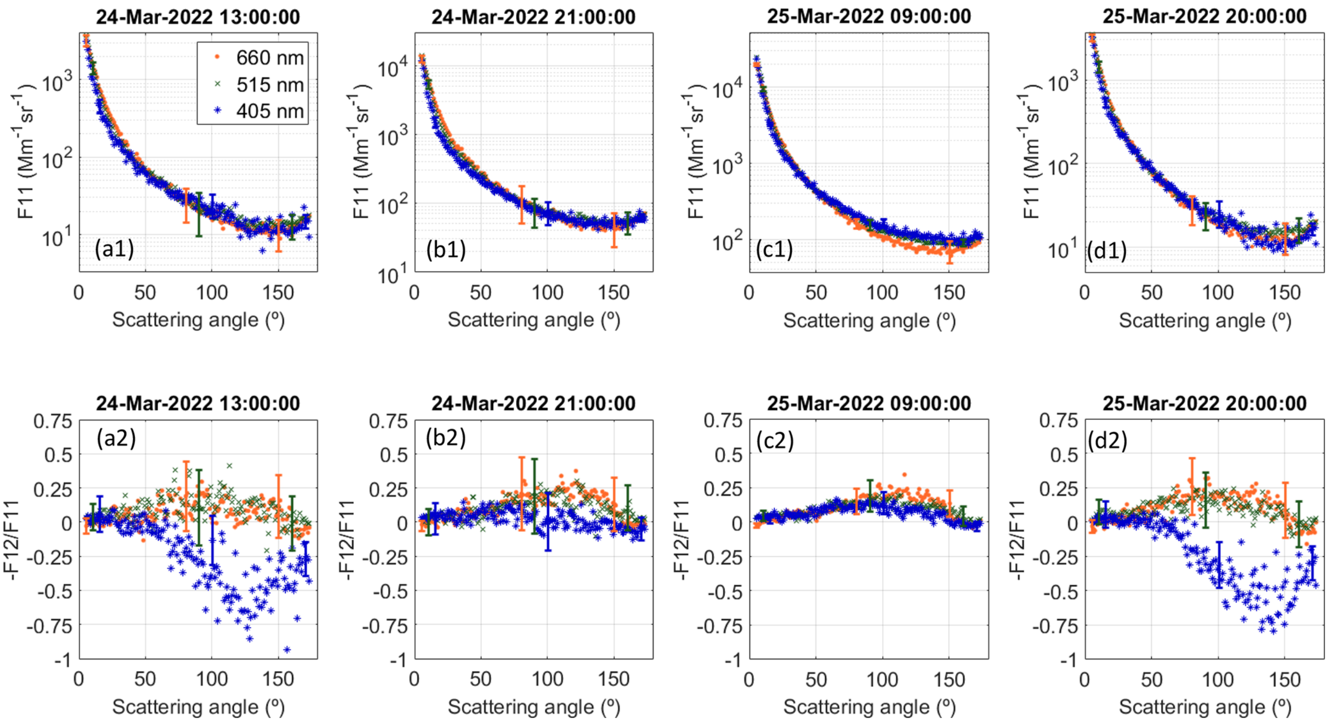

Figure 7. Hourly averages of phase function (F_{11}) and polarized phase function ($-F_{12}/F_{11}$) on 24–25 March 2022 for four different stages of the evolution of the extreme Saharan dust outbreak: **(a)** 24 March at 13:00 UTC before the Saharan dust outbreak reached the station, **(b)** 24 March at 21:00 UTC when the Saharan dust starts to reach the station, **(c)** 25 March at 09:00 UTC associated with the peak of the extreme Saharan dust outbreak, and 25 March at 20:00 UTC when dust begins to withdrawn. Error bars correspond to the standard deviation of the hourly averages.

incides with the maximum of PM_{10}, but the contribution of eBC to the total aerosol burden is lower due to the high concentrations of dust. This can explain the dust-like pattern of $-F_{12}/F_{11}$ at the peak of the event and the general agreement with laboratory measurements of dust samples (Muñoz et al., 2007; Volten et al., 2001).

4.2 Moderate dust events during spring/summer 2022

The PI-Neph also continuously operated from April to September 2022, and other events of Saharan dust transport were recorded at the UGR station. However, these outbreaks did not exhibit such extreme dust transport when compared with the events in March 2022. Actually, hourly averaged PM_{10} levels were below 130 µg m^{-3} and σ_{sca} below 130 Mm^{-1}, which are typical values observed at the UGR station during Saharan dust outbreaks (Lyamani et al., 2010). For this entire period of measurements (14 April to 9 September), Fig. 8 shows hourly averages of PM_{10} and eBC concentrations, $\sigma_{sca}(\lambda)$, SAE, AAE (both calculated in the 405–660 nm range), $g(\lambda)$, $B_s(\lambda)$, SSA(λ) and LR(λ). For the identification of cases with influence of mineral dust particles, data shown in Fig. 8 are filtered out and correspond only to values of SAE < 1, which are used as a proxy for the presence of dust particles in the atmosphere (i.e., Lyamani et al., 2010; Teri et al., 2024).

Figure 8 reveals that the period with the least frequency of dust events was April–June, although the few cases detected show high values of PM_{10} concentrations and the scattering coefficients with SAE values closer to 1, suggesting a high degree of mixture between dust and pollution. Also, this period presents large spectral dependency in g and B_s, with g ranging between 0.5 and 0.7, and B_s ranging from 0.13–0.18, which are typical values more related to non-Saharan dust aerosols (Horvath et al., 2018). Moreover, SSA shows large variability ranging from 0.5 to around 0.9 for all three wavelengths, where the lower limit of the range suggests the presence of absorbing particles in the sample. This is also supported by the AAE with values close to 1, typical of BC.

During the summer season there are more frequent Saharan dust intrusions, which are typical at the UGR station (Pérez-Ramírez, et al., 2016). Generally, there is more variability in all parameters, suggesting more complex mixtures of dust with other particles: the g parameter, which is wavelength dependent, shows very similar values to those obtained during spring but with important variability ranging between 0.55 and 0.75. SAE and AAE show values between 0 and 1 and between 1 and 2, respectively, which are the typical values when there is influence of dust particles in our

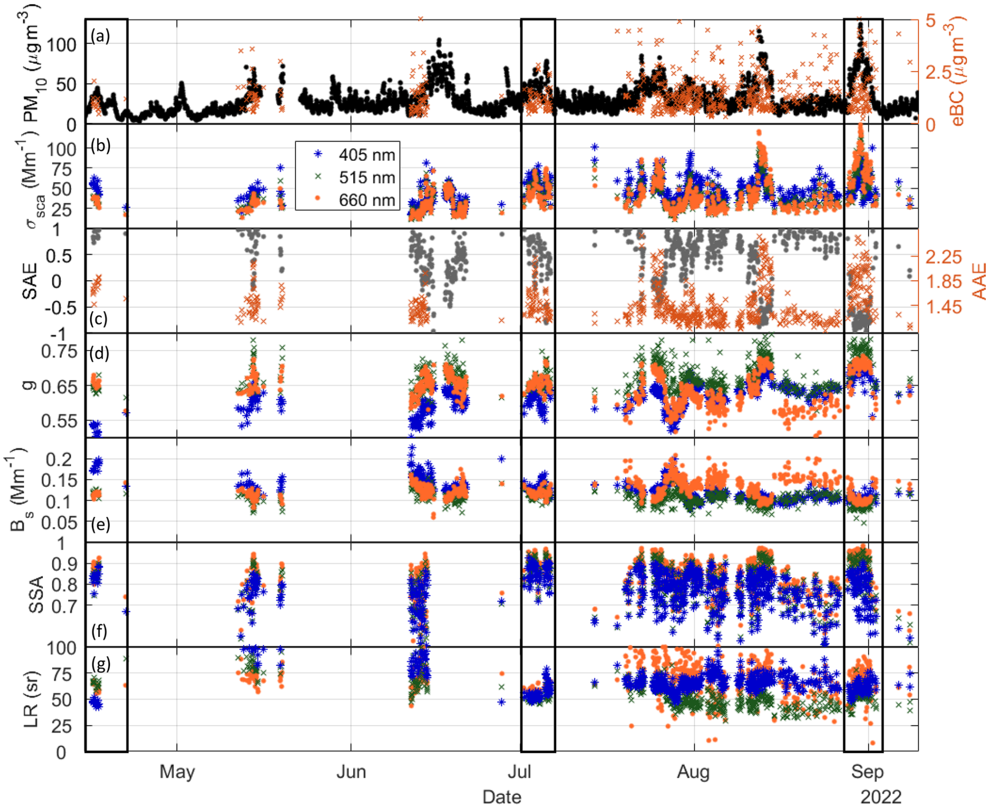

Figure 8. Time series for the moderate dust events of 2022 of the PM$_{10}$ and eBC concentrations (µg m^{-3}) **(a)**, σ_{sca} (scattering coefficient) (Mm^{-1}) **(b)**, SAE (scattering Angström exponent) and AAE (absorption Angström exponent) **(c)**, g (asymmetry parameter) **(d)**, B_s (fraction of backscattered light) (Mm^{-1}) **(e)**, SSA (single scattering albedo) **(f)**, and LR (lidar ratio) (sr) **(g)**. All optical properties are shown at 405, 515 and 660 nm. Black boxes represent three different events on 16 April, 5 July and 30 August 2022.

station (Valenzuela et al., 2015). The outliers in the summer season with negative SAE close to −0.5 and AAE of up to 2.5 might be associated with cases that have more presence of dust. In the summer season the largest values of AAE (close to 2) are observed when compared with the spring season, which can be interpreted as fewer black carbon particles. SSA shows very similar values to those obtained during the spring season.

The LR is a critical variable for backscattered lidar systems and is an intensive aerosol variable that strongly depends on $F_{11}(180°)$ and absorption (Pérez-Ramírez et al., 2019). Because of that, LRs can be very sensitive to the different mixtures of particles in the atmosphere (Burton et al., 2012, 2013; Müller et al., 2007). Results of Fig. 8 serve to illustrate LR variability for dusty conditions but with the influence of other types of particles. Generally, Fig. 8 shows values between 40 and 100 sr for the three wavelengths. The lower limits are closer to the values for large predominance of dust (i.e., Müller et al., 2007), while the upper values are typical values recorded for predominance of smoke/anthropogenic particles (Alados-Arboledas et al., 2011; Burton et al., 2012, 2013; Floutsi et al., 2023; Müller et al., 2007). Thus, results of Fig. 8 indicate the large sensitivity of LR to changes in the mixture of particles. A seasonal analysis indicates that in spring – although there are fewer data – LRs are above 75 sr with little spectral dependence, suggesting more influence of fine particles in the mixture, which are ultimately responsible for LR values. During the summer seasons the lower values around 40–50 sr are more frequent, suggesting more predominance of coarse particles in the mixture.

To gain better understanding of the evolution of the phase matrix elements in different cases of dust mixtures with anthropogenic particles, Fig. 9 shows the phase matrix elements for three different dust events represented by the black boxes in Fig. 8. Particularly, Fig. 9 shows hourly averages of F_{11} and $-F_{12}/F_{11}$ representative of the peak in scattering during each event. Table 2 summarizes hourly mean values of PM$_{10}$ and spectral σ_{sca}, g, B_s, LR and SSA, as well as mean values of SAE and AAE, for these selected cases. The standard deviations are larger (30 % in F_{11} and around 0.2 in $-F_{12}/F_{11}$) when compared with the extreme events, and despite the inherent issues in the measurement of the phase matrix for large particles, it seems that the sample presents a more complex mixture with more variability during the 1 h average.

Table 2. Hourly averaged properties of different dust events in 2022. For properties reported at three wavelengths, the order is 660, 515 and 405 nm (top to bottom). The integration range of σ_{sca} is the angular range of the PI-Neph (5–175°). Error bars are the standard deviations of the hourly means.

	PM_{10} ($\mu g\, m^{-3}$)	eBC ($\mu g\, m^{-3}$)	σ_{sca} (Mm^{-1})	SAE	AAE	g	B_s (Mm^{-1})	SSA	LR (sr)
16 Apr	36 ± 1	0.92 ± 0.14	31 ± 8	0.94 ± 0.88	1.71 ± 0.14	0.641 ± 0.024	0.119 ± 0.014	0.878 ± 0.017	59 ± 14
			31 ± 13			0.630 ± 0.036	0.126 ± 0.017	0.837 ± 0.028	61 ± 17
			48 ± 12			0.505 ± 0.005	0.193 ± 0.001	0.830 ± 0.008	43 ± 5
5 Jul	76 ± 1	1.07 ± 0.11	61 ± 5	-0.46 ± 0.07	1.37 ± 0.13	0.712 ± 0.035	0.097 ± 0.024	0.930 ± 0.004	61 ± 21
			53 ± 5			0.694 ± 0.060	0.109 ± 0.019	0.892 ± 0.016	58 ± 22
			49 ± 2			0.656 ± 0.016	0.114 ± 0.011	0.843 ± 0.007	66 ± 20
30 Aug	124 ± 2	2.42 ± 0.71	129 ± 5	-0.86 ± 0.11	1.73 ± 0.15	0.711 ± 0.019	0.096 ± 0.008	0.920 ± 0.021	67 ± 14
			115 ± 9			0.761 ± 0.021	0.080 ± 0.010	0.882 ± 0.028	58 ± 7
			85 ± 4			0.701 ± 0.009	0.104 ± 0.007	0.789 ± 0.032	63 ± 18

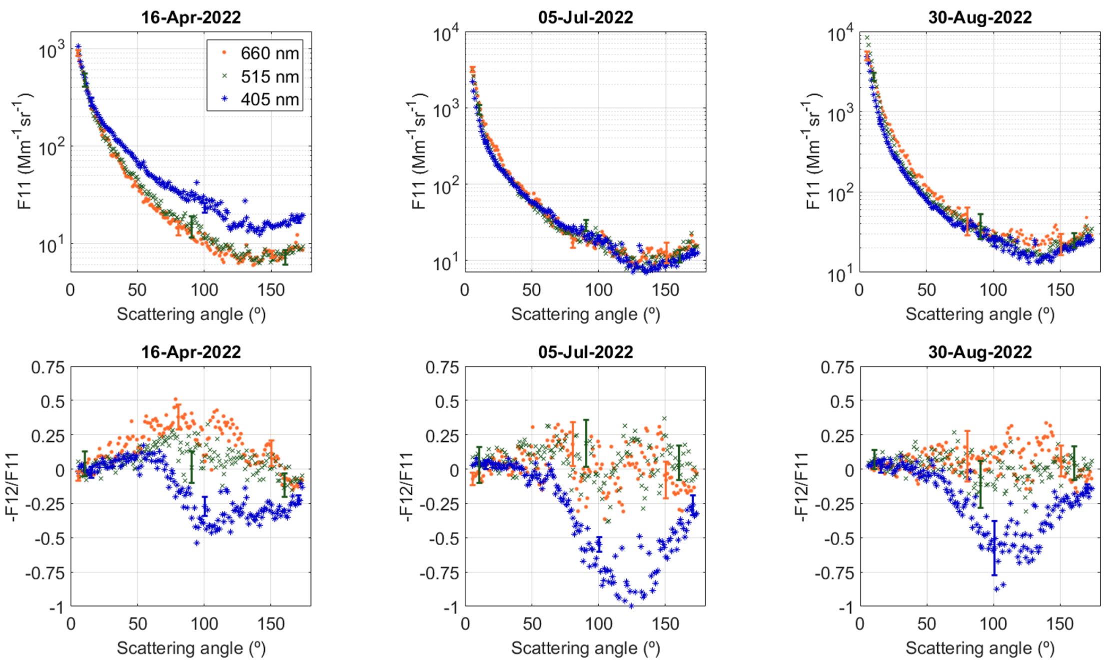

Figure 9. Phase function (F_{11}) and polarized phase function ($-F_{12}/F_{11}$) (for different moderate dust events: 15 April 2022, 25 July 2022 and 30 August 2022). Error bars correspond to the standard deviation of the hourly averages.

The first event on 16 April is one of the most complex in terms of mixture of particles, with the lowest PM_{10} but with the largest SAE and AAE. The values of g suggest the lower contribution of dust particles when compared to the other cases (Horvath et al., 2018). The flat spectral pattern in SSA is the typical observed when there is contribution of fine mode particles of anthropogenic origin during a Saharan dust outbreak (Valenzuela et al., 2014). Nevertheless, the high AAE is not typical of black carbon and thus demonstrates the complexity of the mixture of aerosol particles that day. For the case on 5 July the presence of mineral dust particles seems more relevant. The more pronounced spectral SSA when compared to 16 April also relates to the influence of dust in absorption (Dubovik et al., 2002), although the event on 5 July shows a lower AAE than for the previous case. Finally, the case on 30 August is the one with the largest PM_{10} concentrations but also with the largest eBC, which can make a very complex mixture. However, it should be noted that when affected by high concentrations of dust, the dust particles might interfere with the eBC measurements.

Figure 9 shows that all F_{11} cases exhibit the typical pattern for large and non-spherical particles characterized by large predominance of scattering in the forward region, although there is no remarkable flat behavior of the curve in the backward scattering, which is characteristic of this type of particles from laboratory measurements (i.e., Muñoz et al., 2007).

However, there are differences between the events shown. In the case of the first dust event on 16 April (Fig. 9a), a strong spectral dependency is observed between 405 nm and the other wavelengths from 30° on, which is not observed for the other events. The largest contribution of urban pollution to the mixture could be one of the reasons for these spectral variations on 16 April. Another possible reason could be the smaller influence of absorbing particles as this case also presents the lower eBC and largest SSA when compared with the other two cases. The cases with almost negligible spectral differences could be explained by a greater predominance of large particles. Thus, the discussion of these three selected cases illustrates that even though dust predominant cases present a classical scattering pattern characterized by strong forward scattering, the spectral dependences and the shape of the forward scattering depend ultimately on the mixture of particles. Note that all F_{11} values are coherent with those obtained for the extreme dust outbreaks in March 2022, the agreement being more remarkable for the cases on 5 July and on 30 August.

Measurements of $-F_{12}/F_{11}$ in Fig. 9 present very similar patterns for the three cases. For 515 and 660 nm the $-F_{12}/F_{11}$ patterns are characterized by a bell shape with large variability that might be associated with the complexity of the mixture of mineral dust and anthropogenic particles, as has been also observed for other dust particle measurements in the United States (Espinosa et al., 2018). However, the $-F_{12}/F_{11}$ pattern in 405 nm shows a very different behavior, having $-F_{12}/F_{11}$ positive values until $\sim 70°$ and negative $-F_{12}/F_{11}$ values for the following angles. Minimum $-F_{12}/F_{11}$ values are in the region around 120°. Therefore, $-F_{12}/F_{11}$ measurements can be potentially used for investigating the mixture of particles in the sample. That pattern with negative values has been observed at the UGR station for cases with no influence of Saharan dust particles (Bazo et al., 2024) and for biomass burning at 473 nm (Espinosa et al., 2017). Nevertheless, there are differences between the three different cases that might be associated with the differences in the mixtures of aerosol particles.

5 Discussion

5.1 Comprehensive assessment of the different dust events

To gain more insight about aerosol mixtures during the extreme dust event on 24–25 March 2022 and the rest of dust cases recorded in the period April–September 2022, we use the typing methodology defined in Cazorla et al. (2013) and modified in Schmeisser et al. (2017), based on optical properties. To that end, Fig. 10 shows SAE versus AAE, both parameters being computed in the range 450–700 nm. For the SAE, we have used the σ_{sca} measured with the TSI integrating nephelometer since it directly provides measurements at the same wavelengths than those required in Schmeisser et al. (2017). The different types of aerosols are also illustrated in the figure, where BC refers to black carbon and brown carbon (BrC) to brown carbon in the definitions given by Schmeisser et al. (2017). Different colors are used to identify different stages in the temporal evolution for the extreme dust event on 24–25 March (note that for the event on 15–16 March there were no aethalometer data and thus no measurements of AAE).

Figure 10 shows that for the extreme dust outbreak on 24–25 March 2022, most of the data fall in the region of the pure dust type, particularly those recorded at the beginning of the dust event when the PM_{10} concentrations were extremely high, implying large predominance of coarse mineral dust particles. As the dust event evolves, particularly from 26 March 2022, the data points start to fall in the region of mixed dust/BC/BrC. This coincides with the drop of PM_{10} concentration and the increase of eBC observed in Fig. 5. Therefore, there could be a more balanced contribution of both urban background pollution and mineral dust. If we compare these typing features with the scattering matrix elements on 24–25 March 2022 (Fig. 7), we observe that for the cases typed as pure dust, the $-F_{12}/F_{11}$ follows a bell-shaped pattern for all wavelengths. However, for the cases classified as mixtures, there was a different pattern $-F_{12}/F_{11}$ for the 405 nm channel. Thus, the typing classification explains the differences in the phase matrix for the temporal evolution of the extreme dust events during 15–16 and 24–25 March 2022 at the UGR station and shows the potential of ground-based phase matrix measurements to distinguish between different types of aerosol mixtures.

For the rest of the analyzed period from April to September 2022 (classified as moderate events most in Fig. 8), most of the data fall in the region of the large particle–BC mix and mixed dust/BC/BrC in Fig. 10. Since the UGR station is affected by local pollution (mainly road traffic), it is expected that the dust transported from the Sahara gets mixed with the urban background pollution that is already suspended in the atmosphere. Another possibility is that dust already presents anthropogenic particles injected into the ensemble of particles during the transport process (Querol et al., 2019; Valenzuela et al., 2015). However, going further into the origin of these anthropogenic particles in the mixture is not possible with the current data. In this study, the most important feature is that these possible mixtures can explain the differences in F_{11} and $-F_{12}/F_{11}$ between the extreme and moderate dust events, and also the different situations of dust mixtures in the station.

To further understand the behavior of the optical properties during different dust events, we have performed an average of all moderate dust events of the period April–September 2022 (filtered by SAE < 0.5 to guarantee more dust predominance) and compared it with the peaks of the extreme dust events, i.e., 15 March 2022 at 17:00 UTC and 25 March 2022 at 09:00 UTC. For this purpose, Fig. 11 shows F_{11} and $-F_{12}/F_{11}$ phase matrix elements for the different situations.

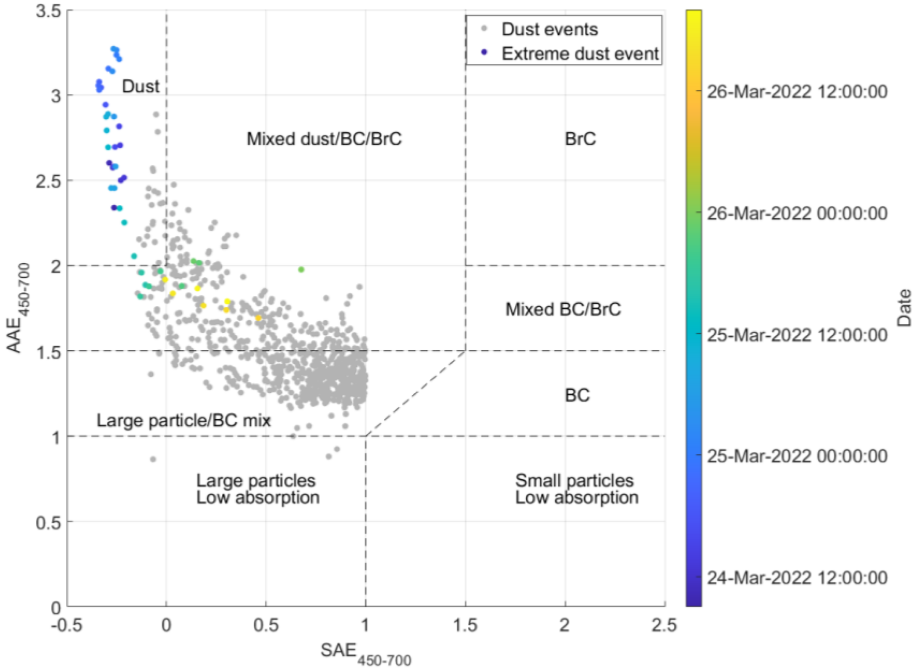

Figure 10. Absorption Angström exponent (AAE) versus scattering Angström exponent (SAE) for the extreme dust event on 24–25 March 2022 (colored markers) and for the moderate dust events recorded at the UGR station during the period April–September 2022 (gray markers). Both intensive properties have been calculated in the range 450–700 nm. Color bar indicates the temporal evolution of the extreme dust event on 24–25 March. Classification of different aerosol types following the method proposed by Schmeisser et al. (2017) is also shown.

For comparisons, we also include laboratory measurements of Saharan dust samples with the polar nephelometer in the Andalusian Institute of Astrophysics (Muñoz et al., 2010), which are available in the Granada–Amsterdam Light Scattering Database (Muñoz et al., 2012). This database provides measurements of F_{11} and $-F_{12}/F_{11}$ at 488 and 632 nm; see Gómez Martín et al. (2021) for details. Results of F_{11} have been normalized with respect to $F_{11}(30°)$ to have the same scale for comparison.

Figure 11 reveals that the F_{11} matrix element presents very similar features for the three wavelengths between mean averages for the period April–September 2022 and the extreme dust events, the difference being within the standard deviations. There are only slight differences in the forward region above 160° scattering angles, particularly for the 515 nm channel, that might be associated by the complexity of the scattering at these angles for large and non-spherical particles (Mischenko et al., 2002; Muñoz et al., 2007). Also, the small standard deviations of F_{11} are remarkable for the mean seasonal values, which suggests that F_{11} follows very similar patterns when there is a predominance of large particles, independently of the mixture with other anthropogenic particles. Moreover, these patterns of F_{11} obtained from ambient aerosol basically coincide with those provided by the Light Scattering Database.

Figure 11 shows that seasonal values of $-F_{12}/F_{11}$ present larger standard deviations when compared to F_{11} in all cases. Particularly, for 660 and 515 nm, large standard deviations are found in the region between 50–150°, while for 405 nm the standard deviations are considerably lower. Apart from the inherent limitations in the measurements in this scattering range, the results suggest that these $-F_{12}/F_{11}$ values at 660 and 515 nm are very sensitive to changing conditions in the aerosol that is sampled. Moreover, the other region that presents remarkable standard deviations for all wavelengths is the region of scattering angles above 170°. Those regions with large standard deviations are very sensitive to any change in particle type and size, which was demonstrated both from theoretical computations (Mischenko et al., 2002) and in laboratory measurements (Gómez Martín et al., 2021). However, the lower standard deviations observed for the 405 nm wavelength indicate homogeneity in the response to polarization, even in the presence of other anthropogenic particles in the sample.

The comparison of means $-F_{12}/F_{11}$ between the different situations reveals very important features. Specifically, for 660 nm, F_{12}/F_{11} follows a very similar pattern between the extreme events and the Light Scattering Database. The mean seasonal average also follows the same pattern but with a lower maximum and displaced to lower scattering regions. However, the 405 nm channel presents the most different behavior between the seasonal averages and the phase matrix elements for dust events with two different patterns: for the extreme dust events and the Light Scattering Database, there

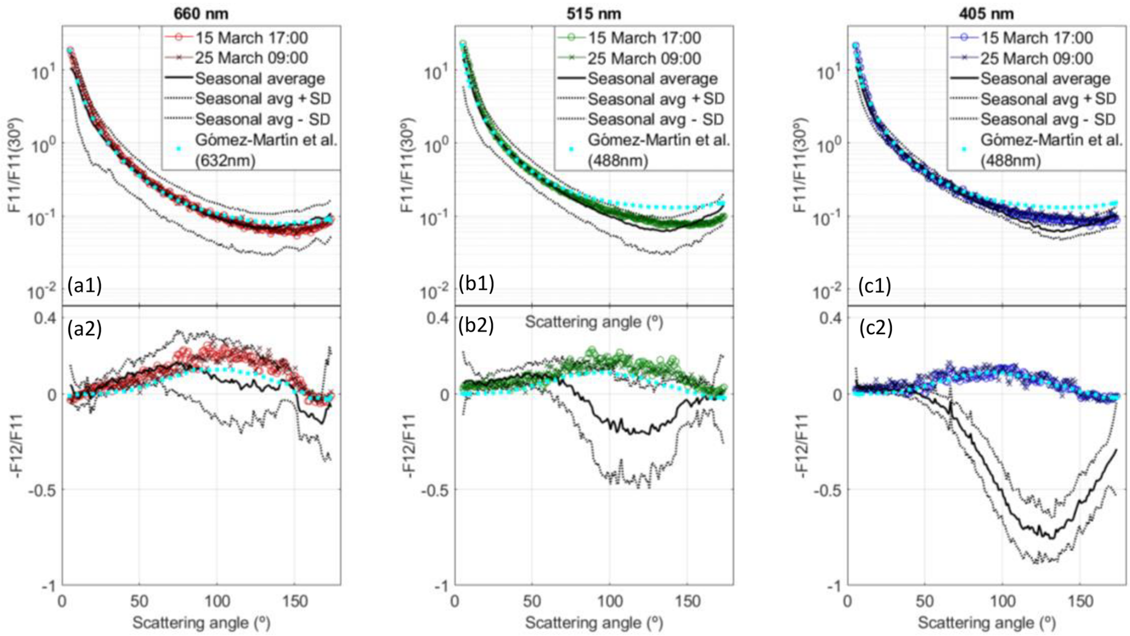

Figure 11. Phase function (F_{11}) (**a**1–**c**1) and polarized phase function ($-F_{12}/F_{11}$) (**b**1–**c**1) for different situations: Mean values for the cases obtained during moderate dust events (black lines), cases for extreme events on 15 March 2022 (red open circles) and on 25 March 2022 (red stars), and laboratory measurements at 632 and 488 nm (light-blue dots) with samples collected in the Sahara and available in the Granada–Amsterdam Light Scattering Database (Muñoz et al., 2012).

is a bell-shaped pattern with values close to zero and a maximum of 0.1 at 100°, the differences between both sets of data being negligible. A different pattern is observed for the seasonal average, characterized by values around zero up to 50°, decreasing later to a minimum of −0.7 at 120° and increasing again to values close to 0 in the backward scattering region. Finally, the 515 nm channel presents an intermedia situation, the extreme dust cases and the Light Scattering Database at 488 nm patterns being very similar, while for the average of usual dust cases, the pattern is like that observed at 405 nm but with less pronounced negative values.

The overall analysis of F_{11} and $-F_{12}/F_{11}$ phase matrix elements reveals that F_{11} patterns and spectral dependence are strongly affected by the existence of large and non-spherical particles, the existence of other anthropogenic particles in the mixture mainly affecting the backscattering region. However, the possible existence of anthropogenic particles in the ensemble of particles characterized by the predominance of large and non-spherical particles can importantly affect the values of $-F_{12}/F_{11}$ with strong wavelength dependence. These changes are critical in the 405 nm channel, the $-F_{12}/F_{11}$ negative values being like those observed for pollution (i.e., Bazo et al., 2024) and biomass burning at 473 nm (i.e., Espinosa et al., 2017). The 515 and 660 nm channels show $-F_{12}/F_{11}$ patterns more typical of pure dust measurements at laboratory (Muñoz et al., 2007; Renard et al., 2010). Therefore, polarization measurements have great potential for distinguishing different aerosol types in the mixture, which can be either internal or external mixtures of dust with other types of particles. Some model simulations even suggest that non-absorptive coating in mineral dust has a drastic variation in the behavior of $-F_{12}/F_{11}$ (Zhang et al., 2022, 2023), such as coatings of non-absorptive aerosol due to the long-range transport (Dall'Osto et al., 2010). Future works will focus on detailed studies of chemical analyses in combination with polar nephelometry measurements to further exploit the potential of polarization measurements in aerosol studies.

5.2 Phase matrix simulations for different aerosol mixture scenarios

To fully understand how different degrees of mixture between anthropogenic particles and mineral dust can affect F_{11} and $-F_{12}/F_{11}$, forward simulations with the Generalized Retrieval of Aerosol and Surface Properties algorithm (GRASP; Dubovik et al., 2014, 2021) have been performed. These simulations need inputs of different size distributions and refractive indexes to generate F_{11} and $-F_{12}/F_{11}$. In particular, we used a bi-lognormal size distribution, one representative of fine-mode particles with a modal radius of 0.15 and 0.25 µm of standard deviation and the other representative of coarse-mode particles with a modal radius of 2.5 and 1 µm of standard deviation. Real refractive indexes were assumed non-spectrally dependent, with values of 1.6 for the fine mode and 1.55 for the coarse mode. Imaginary refractive indexes were 0.0015 for the fine mode and with no spectral dependency, while for the coarse mode there were 0.007, 0.005 and 0.005 for 405, 515 and 660 nm. The spherical fraction was also fixed for each mode, being 0.7 for the fine mode and 0.05 for the coarse mode. The modal radii selected are close to those observed for the particle size distribution of the deposited particles at the UGR station (not shown for clarity). Moreover, the size distribution and refractive indexes selected can be considered representative of a mixture of anthropogenic pollution and dust (Torres et al., 2017). Three different scenarios were generated giving different weights to each mode: the first is for volume concentrations of 0.3 $\mu m^3\,\mu m^{-3}$ for each mode and can be considered representative of a mixed case, where both modes have a similar weight. The second presents more predominance of the coarse mode (volume concentration of 0.5 $\mu m^3\,\mu m^{-3}$ for the coarse mode) but with non-negligible contribution of anthropogenic particles (volume concentrations of 0.1 $\mu m^{-3}\,\mu m^{-3}$ for the fine mode). The last scenario is representative of the pure dust mode (volume concentrations of 0.5 $\mu m^3\,\mu m^{-3}$), with a negligible fine-mode contribution (volume concentrations of 0.01 $\mu m^3\,\mu m^{-3}$). Results of computed F_{11} and $-F_{12}/F_{11}$ are in Fig. 12.

Figure 12 reveals important features in phase matrix elements depending on the mixture. For F_{11}, the patterns are generally characterized by larger forward scattering, with minima in the region of 120–150°, independent of the type of aerosol mixture and the wavelength. The largest spectral dependencies are for the *Urban mixture* case, while for the other two cases such spectral dependencies become negligible. However, for $-F_{12}/F_{11}$ the largest variations in spectral dependencies and patterns are observed. In the Urban mixture case, the 660 nm channel shows a bell-shaped pattern with a maximum of ~ 0.4 in the region around 100°, while for 405 nm $-F_{12}/F_{11}$ shows approximately constant values close to zero until $\sim 50°$, when it starts to decrease until the minimum of –0.5 in the region $\sim 140°$. Later it recovers, reaching zero at 180°. On the other hand, for *Pure dust* the $-F_{12}/F_{11}$ spectral dependencies are almost negligible, and it is characterized by a bell-shaped pattern with a maximum around 0.2 in the region 110–130°, with small negative values around 180°. Note that this feature is also present in the $-F_{12}/F_{11}$ in Fig. 11 for the extreme dust cases, but it is not noticeable due to the scale. For the *Dust mixed* combination, the pattern is between the previous ones.

Figure 12 results show how the presence of anthropogenic particles (fine mode) can alter the spectral dependencies in $-F_{12}/F_{11}$ when compared with only dust particles (coarse mode) in the sample, particularly in the blue channels. However, changes in the F_{11} patterns were not so evident. These results help to understand the different phase matrix elements discussed in this paper and their temporal evolutions during the extreme dust events (Supplement). However, studying the relationships between measured F_{11} and $-F_{12}/F_{11}$ with other aerosol optical and microphysical properties requires further analyses because F_{11} and $-F_{12}/F_{11}$ ultimately depend on the size distribution, refractive indexes and particle shapes. The problem is even more complex if we differentiate optical properties between fine and coarse mode. Future optimization in GRASP will permit the retrieval of aerosol refractive indexes between fine and coarse mode separately using F_{11} and $-F_{12}/F_{11}$ as inputs, thus permitting further analyses of the different study cases discussed in this work. It is important to mention that the super-coarse mode can also affect the behavior of F_{11} and $-F_{12}/F_{11}$, and the presence of this mode is also observed for long-range transport (i.e., Renard et al., 2010). Future GRASP development also needs the consideration of this super-coarse mode. Another issue to study is the use of a irregular-hexahedral model for modeling the scattering of large and non-spherical particles that might reproduce better polarization signals (Saito and Yang, 2021, 2023; Saito et al., 2021).

6 Conclusions

This work has focused on the analyses of aerosol phase matrix elements and other optical properties during Saharan dust outbreaks that were recorded at the UGR station (southeastern Spain) in the year 2022. The main novelty of the analyses is the measurements by a multiwavelength polarized imaging nephelometer (PI-Neph) developed by GRASP-Earth, capable of providing two aerosol scattering matrix elements (F_{11} and $-F_{12}/F_{11}$) for three different wavelengths (405, 515 and 660 nm). The uniqueness of PI-Neph is that it allows us to measure phase matrix elements of ambient aerosol. The optimization of the instrument and the data quality check applied served to obtain F_{11} and $-F_{12}/F_{11}$ with uncertainties below 10 % and 20 %, respectively. The multiwavelength F_{11} and $-F_{12}/F_{11}$ measurements for different Saharan dust outbreaks are some of the first carried out for ambient aerosol particles and serve to complement laboratory measurements of mineral dust particles and of synthetic samples minerals that compose dust particles. The novel measurements of F_{11} and $-F_{12}/F_{11}$ can also complement other optical and microphysical properties of Saharan dust already known from in situ instrumentation and by active and passive remote sensing instruments, from both the ground and space.

The analyses differentiate between two different scenarios: the first is two extreme Saharan dust outbreaks that happened on 15–16 March (peaks in PM_{10} $\sim 1800\,\mu g\,m^{-3}$) and on 25–26 March 2022 (peaks in PM_{10} $\sim 690\,\mu g\,m^{-3}$) when the daily limit value of 50 $\mu g\,m^{-3}$ delimited by the 2008/50/CE European Directive was exceeded. The detailed temporal evolution analysis of F_{11} for these extreme events did not show relevant changes with time, showing the classical pattern for predominance of big and non-spherical particles characterized by a high predominance of forward scattering and almost negligible wavelength differences. For $-F_{12}/F_{11}$ at 515 and 660 nm there were no remarkable differences with

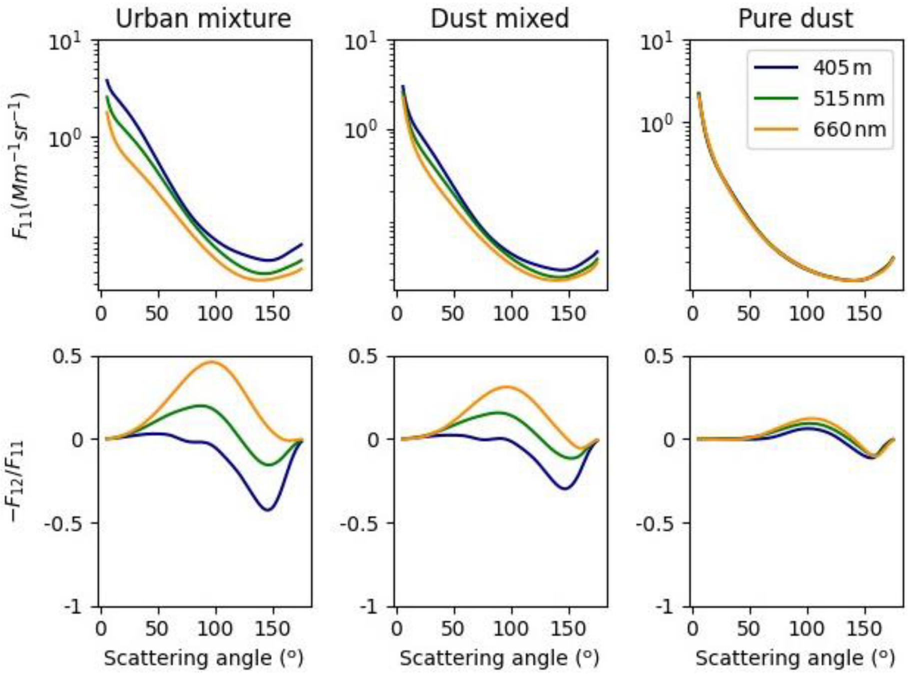

Figure 12. Simulations of phase function (F_{11}) and polarized phase function ($-F_{12}/F_{11}$) using GRASP forward for three different combinations of bi-lognormal size distributions. Urban mixture with approximately the same weight of fine and coarse mode, Dust mixed with predominance of coarse mode but with a non-negligible influence of the fine mode, and Pure dust with strong predominance of coarse mode and negligible fine mode. Note that refractive indexes and sphericity of each mode are different.

time, showing a bell-shaped pattern centered at $\sim 90°$ and with slightly positive values (maxima ~ 0.2). However, for 405 nm this bell-shaped pattern was only present for the instants of extreme predominance of dust, while for the other instants $-F_{12}/F_{11}$ showed a very different pattern, with values close to zero up to 50–60°, followed by a decrease to values between -0.4 and -0.6 in the region around 120° and a final increase, recovering to values close to zero in the backward region. On the other hand, the second analysis scenario was the period April–September 2022 when more moderate Saharan dust intrusions were recorded (maximum PM_{10} around 100 $\mu g\, m^{-3}$). F_{11} mostly followed the classical pattern characterized by strong forward scattering, although some cases showed some spectral dependence on 405 nm depending on the influence of fine-mode particles in the mixture. However, the analysis of $-F_{12}/F_{11}$ revealed big differences among wavelengths, being 405 nm like the pattern observed during the moments prior to and after the peaks of the extreme dust events. The typing classification with additional in situ measurements classified the peaks of the extreme dust events as pure dust, while for the rest of measurements a mixture of dust particles with local anthropogenic pollution was indicated, which could be the reason for the differences in $-F_{12}/F_{11}$. Thus, polarization at 405 nm seems to be very sensitive to the presence of additional anthropogenic particles in the sample dominated by mineral dust. For 515 and 660 nm there is large variability depending on the mixture of particles. Nevertheless, more F_{11} and $-F_{12}/F_{11}$ measurements are needed at other experimental sites to have a more complete vision of mineral dust role on climate.

Laboratory measurements of mineral dust samples available in the Granada–Amsterdam Light Scattering Database provided F_{11} and $-F_{12}/F_{11}$ at 488 and 632 nm, allowing for a comparative assessment. To that end, averages of the period April–September 2022 and the peaks of the extreme events during March 2022 were used. The results showed that for all normalized F_{11} values, the differences between temporal averages, peak events and laboratory measurements were minimal, being only notable in the backscattering region close to 180°, where according to the T-matrix theory more sensitivity to aerosol particle parameters is found. For $-F_{12}/F_{11}$ laboratory measurements showed a bell-shaped pattern with maxima around 0.2 in the region $\sim 90°$, both at 488 and 632 nm, indicating very good agreement with the PI-Neph seasonal averages at 660 nm but important departures when compared with 405 nm. However, during the peaks of the extreme dust events $-F_{12}/F_{11}$ comparisons with laboratory measurements agree quite well. Considering that laboratory measurements consist of pure dust samples directly collected in the desert, we can conclude that the $-F_{12}/F_{11}$ at 405 nm measured in the laboratory is only reproduced when there are extreme concentrations of dust in the atmosphere, while $-F_{12}/F_{11}$ is critically affected by the contribution of anthropogenic particles in the mixture. For the other channels, particularly 660 nm, $-F_{12}/F_{11}$ seems to be less critically affected by the contribution of anthropogenic particles. We therefore believe that multiwavelength-polarized polar nephelometry opens new possibilities in the studies of mineral dust role in the climate system.

Simulations performed by the GRASP code for different mixtures of the fine mode (anthropogenic particles) and coarse mode (dust particles) revealed that F_{11} and $-F_{12}/F_{11}$ are sensitive to the different contribution of each mode in the mixture, being especially critical for $-F_{12}/F_{11}$ in the 405 nm channel. The negative values for $-F_{12}/F_{11}$ in 405 nm were observed more clearly for the mixture of fine and coarse particles. Thus, these simulations have served to understand the experimental negative values in $-F_{12}/F_{11}$, not observed in laboratory measurements for collected dust. Retrievals of bimodal size distribution with separate refractive indexes for each mode would have shown clarity for this problem. However, such retrieval with GRASP using F_{11} and $-F_{12}/F_{11}$ as inputs needs to be optimized. Another additional optimization in GRASP will provide the possibility of implementing the retrieval of super-coarse-mode particles. The possibility of implementing the irregular-hexahedral model would also be ideal to better understand polarization patterns. Nevertheless, the possibility of explaining the spectral differences in F_{11} and $-F_{12}/F_{11}$ with wavelength has served to understand the temporal evolution of the extreme dust events and the difference and similitudes when comparing versus laboratory measurements and versus other more moderate events of Saharan dust transport. However, going further in understanding the interaction of dust with these anthropogenic particles requires further analyses that provide the chemical composition and size distribution of the ensemble of particles. This is planned in future studies that will allow a more complete comprehensive analysis.

Code and data availability. Code and data will be available upon request.

Supplement. The supplement related to this article is available online at https://doi.org/10.5194/acp-25-6325-2025-supplement.

Author contributions. EB analyzed the data and wrote the manuscript. DPR and FJO defined the structure of the paper, conceptualized the investigation and supervised the writing of the manuscript. ADZ analyzed the meteorological conditions during the extreme Saharan dust outbreaks. FR performed the GRASP simulations. FJO, AV and LAA are the principal investigators of the projects that funded the research and put the guidelines of the research. GT, AC, DP and FJGI assisted in the conceptualization. JVM and DF contributed to the development of the instrumentation. All authors contributed to the discussion of the results and provided comments on the paper.

Competing interests. The contact author has declared that none of the authors has any competing interests.

Disclaimer. Publisher's note: Copernicus Publications remains neutral with regard to jurisdictional claims made in the text, published maps, institutional affiliations, or any other geographical representation in this paper. While Copernicus Publications makes every effort to include appropriate place names, the final responsibility lies with the authors.

Acknowledgements. This work was supported mainly by the Horizon Europe program under the Marie Skłodowska-Curie Staff Exchange Actions with the project GRASP-SYNERGY (grant agreement no. 101131631). The work was also funded by the European Union's Horizon 2020 research and innovation program through projects ACTRIS.IMP (grant agreement no. 871115) and ATMO_ACCESS (grant agreement no. 101008004); by the Spanish Ministry of Science and Innovation through projects ELPIS (PID2020-12001-5RB-I00), MULHACEN (PID2021-128008OB-I00) and NUCLEUS (PID2021-128757OB-I00), funded by MICIU/AEI/10.13039/501100011033 and ERDF through "A way of making Europe" and ACTRIS-España (RED2022-134824-E); and by the University of Granada Plan Propio through the Excellence Research Unit Earth Science and Singular Laboratory AGORA (LS2022-1) programs. Elena Bazo received funding by MICIU/AEI/10.13039/501100011033 and the ESF+ through FPI fellowship PRE2022-101272. Francisco José García-Izquierdo acknowledges financial support from the grant PID2021-123370OB-I00 (CATS), funded by MCIN/AEI/10.13039/501100011033. We are very thankful to the Air Quality Service of Junta de Andalucía for supplying the PM_{10} data.

Financial support. This work was supported by the EU Horizon Europe program under the Marie Sklodowska-Curie Staff Exchange Actions with the project GRASP-SYNERGY (grant agreement no. 101131631) and by the Spanish Minestry of Science and Innovation through the project MULHACEN (PID2021-12800OBI00).

Review statement. This paper was edited by Matthias Tesche and reviewed by two anonymous referees.

References

Adebiyi, A. A. and Kok, J. F.: Climate models miss most of the coarse dust in the atmosphere, Sci. Adv., 6, https://doi.org/10.1126/sciadv.aaz9507, 2020.

Adebiyi, A., Kok, J. F., Murray, B. J., Ryder, C. L., Stuut, J. B. W., Kahn, R. A., Knippertz, P., Formenti, P., Mahowald, N. M., Pérez García-Pando, C., Klose, M., Ansmann, A., Samset, B. H., Ito, A., Balkanski, Y., Di Biagio, C., Romanias, M. N., Huang, Y., and Meng, J.: A review of coarse mineral dust in the Earth system, Aeolian Res., 60, 100849, https://doi.org/10.1016/j.aeolia.2022.100849, 2023.

Ahern, A. T., Erdesz, F., Wagner, N. L., Brock, C. A., Lyu, M., Slovacek, K., Moore, R. H., Wiggins, E. B., and Murphy, D. M.: Laser imaging nephelometer for aircraft deployment, Atmos. Meas. Tech., 15, 1093–1105, https://doi.org/10.5194/amt-15-1093-2022, 2022.

Alados-Arboledas, L., Müller, D., Guerrero-Rascado, J. L., Navas-Guzmán, F., Pérez-Ramírez, D., and Olmo, F. J.: Optical and microphysical properties of fresh biomass burning aerosol retrieved by Raman lidar, and star-and sun-photometry, Geophys. Res. Lett., 38, L01807, https://doi.org/10.1029/2010GL045999, 2011.

Anderson, T. L., Covert, D. S., Marshall, S. F., Laucks, M. L., Charlson, R. J., Waggoner, A. P., Ogren, J. A., Caldow, R., Holm, R. L., Quant, F. R., Sem, G. J., Wiedensohler, A., Ahlquist, N. A., and Bates, T. S.: Performance Characteristics of a High-Sensitivity, Three-Wavelength, Total Scatter/Backscatter Nephelometer, J. Atmos. Ocean. Tech., 13, 967–986, https://doi.org/10.1175/1520-0426(1996)013<0967:PCOAHS>2.0.CO;2, 1996.

Anderson, T. L. and Ogren, J. A.: Determining Aerosol Radiative Properties Using the TSI 3563 Integrating Nephelometer, Aerosol Sci. Tech., 29, 57–69, https://doi.org/10.1080/02786829808965551, 1998.

Barkey, B., Liou, K. N., Gellerman, W., and Sokolsky, P.: An Analog Light Scattering Experiment of Hexagonal Icelike Particles. Part I: Experimental Apparatus and Test Measurements, J. Atmos. Sci., 56, 605–612, https://doi.org/10.1175/1520-0469(1999)056<0605:AALSEO>2.0.CO;2, 1999.

Bazo, E., Granados-Muñoz, M. J., Román, R., Bravo-Aranda, J. A., Cazorla, A., Valenzuela, A., González, R., Olmo, F. J., and Alados-Arboledas, L.: Evaluation of the vertically-resolved aerosol radiative effect on shortwave and longwave ranges using sun-sky photometer and ceilometer measurements, Atmos. Res., 282, 106517, https://doi.org/10.1016/j.atmosres.2022.106517, 2023.

Bazo, E., Martins, J. V., Perez-Ramirez, D., Valenzuela, A., Titos, G., Cazorla, A., Fuertes, D., Weiss, M., Turpie, A., Li, C., García-Izquierdo, F. J., Foyo-Moreno, I., Alados-Arboledas, L., and Olmo, F. J.: Optimization of the Polarized Imaging Nephelometer (PI-Neph) for continuous monitoring of multiwavelength aerosol phase functions in support of space polarimetry missions, Atmos. Environ., 316, 120181, https://doi.org/10.1016/j.atmosenv.2023.120181, 2024.

Benedetti, A., Morcrette, J. -J., Boucher, O., Dethof, A., Engelen, R. J., Fisher, M., Flentje, H., Huneeus, N., Jones, L., Kaiser, J. W., Kinne, S., Mangold, A., Razinger, M., Simmons, A. J., and Suttie, M.: Aerosol analysis and forecast in the European Centre for Medium-Range Weather Forecasts Integrated Forecast System: 2. Data assimilation, J. Geophys. Res.-Atmos., 114, D13205, https://doi.org/10.1029/2008JD011115, 2009.

Berkoff, T. A., Sorokin, M., Stone, T., Eck, T. F., Hoff, R., Welton, E., and Holben, B.: Nocturnal aerosol optical depth measurements with a small-aperture automated photometer using the moon as a light source, J. Atmos. Ocean. Tech., 28, 1297–1306, https://doi.org/10.1175/JTECH-D-10-05036.1, 2011.

Bian, Y., Zhao, C., Xu, W., Zhao, G., Tao, J., and Kuang, Y.: Development and validation of a CCD-laser aerosol detective system for measuring the ambient aerosol phase function, Atmos. Meas. Tech., 10, 2313–2322, https://doi.org/10.5194/amt-10-2313-2017, 2017.

Bodhaine, B. A., Ahlquist, N. C., and Schnell, R. C.: Three-wavelength nephelometer suitable for aircraft measurement of background aerosol scattering coefficient, Atmos. Environ., 25, 2267–2276, https://doi.org/10.1016/0960-1686(91)90102-D, 1991.

Burton, S. P., Ferrare, R. A., Hostetler, C. A., Hair, J. W., Rogers, R. R., Obland, M. D., Butler, C. F., Cook, A. L., Harper, D. B., and Froyd, K. D.: Aerosol classification using airborne High Spectral Resolution Lidar measurements – methodology and examples, Atmos. Meas. Tech., 5, 73–98, https://doi.org/10.5194/amt-5-73-2012, 2012.

Burton, S. P., Ferrare, R. A., Vaughan, M. A., Omar, A. H., Rogers, R. R., Hostetler, C. A., and Hair, J. W.: Aerosol classification from airborne HSRL and comparisons with the CALIPSO vertical feature mask, Atmos. Meas. Tech., 6, 1397–1412, https://doi.org/10.5194/amt-6-1397-2013, 2013.

Casquero-Vera, J. A., Lyamani, H., Titos, G., Minguillón, M. C., Dada, L., Alastuey, A., Querol, X., Petäjä, T., Olmo, F. J., and Alados-Arboledas, L.: Quantifying traffic, biomass burning and secondary source contributions to atmospheric particle number concentrations at urban and suburban sites, Sci. Total Environ., 768, 145282, https://doi.org/10.1016/j.scitotenv.2021.145282, 2021.

Casquero-Vera, J. A., Pérez-Ramírez, D., Lyamani, H., Rejano, F., Casans, A., Titos, G., Olmo, F. J., Dada, L., Hakala, S., Hussein, T., Lehtipalo, K., Paasonen, P., Hyvärinen, A., Pérez, N., Querol, X., Rodríguez, S., Kalivitis, N., González, Y., Alghamdi, M. A., Kerminen, V.-M., Alastuey, A., Petäjä, T., and Alados-Arboledas, L.: Impact of desert dust on new particle formation events and the cloud condensation nuclei budget in dust-influenced areas, Atmos. Chem. Phys., 23, 15795–15814, https://doi.org/10.5194/acp-23-15795-2023, 2023.

Cazorla, A., Bahadur, R., Suski, K. J., Cahill, J. F., Chand, D., Schmid, B., Ramanathan, V., and Prather, K. A.: Relating aerosol absorption due to soot, organic carbon, and dust to emission sources determined from in-situ chemical measurements, Atmos. Chem. Phys., 13, 9337–9350, https://doi.org/10.5194/acp-13-9337-2013, 2013.

Cazorla, A., Casquero-Vera, J. A., Román, R., Guerrero-Rascado, J. L., Toledano, C., Cachorro, V. E., Orza, J. A. G., Cancillo, M. L., Serrano, A., Titos, G., Pandolfi, M., Alastuey, A., Hanrieder, N., and Alados-Arboledas, L.: Near-real-time processing of a ceilometer network assisted with sun-photometer data: monitoring a dust outbreak over the Iberian Peninsula, Atmos. Chem. Phys., 17, 11861–11876, https://doi.org/10.5194/acp-17-11861-2017, 2017.

Cuevas-Agulló, E., Barriopedro, D., García, R. D., Alonso-Pérez, S., González-Alemán, J. J., Werner, E., Suárez, D., Bustos, J. J., García-Castrillo, G., García, O., Barreto, Á., and Basart, S.: Sharp increase in Saharan dust intrusions over the western Euro-Mediterranean in February–March 2020–2022 and associated atmospheric circulation, Atmos. Chem. Phys., 24, 4083–4104, https://doi.org/10.5194/acp-24-4083-2024, 2024.

Curtis, D. B., Aycibin, M., Young, M. A., Grassian, V. H., and Kleiber, P. D.: Simultaneous measurement of light-scattering properties and particle size distribution for aerosols: Application to ammonium sulfate and quartz aerosol particles, Atmos. Environ., 41, 4748–4758, https://doi.org/10.1016/j.atmosenv.2007.03.020, 2007.

Curtis, D. B., Meland, B., Aycibin, M., Arnold, N. P., Grassian, V. H., Young, M. A., and Kleiber, P. D.: A laboratory investigation of light scattering from representative components of mineral dust aerosol at a wavelength of 550 nm, J. Geophys. Res.-Atmos., 113, D08210, https://doi.org/10.1029/2007JD009387, 2008.

Dall'Osto, M., Harrison, R. M., Highwood, E. J., O'Dowd, C., Ceburnis, D., Querol, X., and Achterberg, E. P.: Variation of the mixing state of Saharan dust particles with atmospheric transport, Atmos. Environ., 44, 3135–3146, https://doi.org/10.1016/j.atmosenv.2010.05.030, 2010.

Daugeron, D., Renard, J.-B., Gaubicher, B., Couté, B., Hadamcik, E., Gensdarmes, F., Basso, G., and Fournier, C.: Scattering properties of sands. 1. Comparison between different techniques of measurements, Appl. Opt., 45, 8331–8337, https://doi.org/10.1364/OA_License_v1#VOR, 2006.

Deuzé, J. L., Bréon, F. M., Deschamps, P. Y., Devaux, C., Herman, M., Podaire, A., and Roujean, J. L.: Analysis of the POLDER (POLarization and directionality of earth's reflectances) airborne instrument observations over land surfaces, Remote Sens. Environ., 45, 137–154, https://doi.org/10.1016/0034-4257(93)90038-Y, 1993.

Di Biagio, C., Formenti, P., Balkanski, Y., Caponi, L., Cazaunau, M., Pangui, E., Journet, E., Nowak, S., Caquineau, S., Andreae, M. O., Kandler, K., Saeed, T., Piketh, S., Seibert, D., Williams, E., and Doussin, J.-F.: Global scale variability of the mineral dust long-wave refractive index: a new dataset of in situ measurements for climate modeling and remote sensing, Atmos. Chem. Phys., 17, 1901–1929, https://doi.org/10.5194/acp-17-1901-2017, 2017.

Di Biagio, C., Formenti, P., Balkanski, Y., Caponi, L., Cazaunau, M., Pangui, E., Journet, E., Nowak, S., Andreae, M. O., Kandler, K., Saeed, T., Piketh, S., Seibert, D., Williams, E., and Doussin, J.-F.: Complex refractive indices and single-scattering albedo of global dust aerosols in the shortwave spectrum and relationship to size and iron content, Atmos. Chem. Phys., 19, 15503–15531, https://doi.org/10.5194/acp-19-15503-2019, 2019.

Dolgos, G. and Martins, J. V.: Polarized Imaging Nephelometer for in situ airborne measurements of aerosol light scattering, Opt. Express, 22, 21972, https://doi.org/10.1364/oe.22.021972, 2014.

Drinovec, L., Močnik, G., Zotter, P., Prévôt, A. S. H., Ruckstuhl, C., Coz, E., Rupakheti, M., Sciare, J., Müller, T., Wiedensohler, A., and Hansen, A. D. A.: The "dual-spot" Aethalometer: an improved measurement of aerosol black carbon with realtime loading compensation, Atmos. Meas. Tech., 8, 1965–1979, https://doi.org/10.5194/amt-8-1965-2015, 2015.

Dubovik, O., Fuertes, D., Litvinov, P., Lopatin, A., Lapyonok, T., Doubovik, I., Xu, F., Ducos, F., Chen, C., Torres, B., Derimian, Y., Li, L., Herreras-Giralda, M., Herrera, M., Karol, Y., Matar, C., Schuster, G. L., Espinosa, R., Puthukkudy, A., Li, Z., Fishcer, J., Preusker, R., Cuesta, J., Kreuter, A., Cede, A., Aspetsberger, M., Marth, D., Bindreiter, L., Hangler, A., Lanzinger, V., Holter, C., and Federspiel, C.: A Comprehensive Description of Multi- Term LSM for Applying Multiple a Priori Constraints in Prob50 lems of Atmospheric Remote Sensing: GRASP Algorithm, Concept, and Applications, Front. Remote Sens., 2, 706851, https://doi.org/10.3389/frsen.2021.706851, 2021.

Dubovik, O., Holben, B., Eck, T. F., Smirnov, A., Kaufman, Y. J., King, M. D., Tanré, D., and Slutsker, I.: Variability of Absorption and Optical Properties of Key Aerosol Types Observed in Worldwide Locations, J. Atmos. Sci., 59, 590–608, https://doi.org/10.1175/1520-0469(2002)059<0590:VOAAOP>2.0.CO;2, 2002.

Dubovik, O. and King, M. D.: A flexible inversion algorithm for retrieval of aerosol optical properties from Sun and sky radiance measurements, J. Geophys. Res.-Atmos., 105, 20673–20696, https://doi.org/10.1029/2000JD900282, 2000.

Dubovik, O., Lapyonok, T., Litvinov, P., Herman, M., Fuertes, D., Ducos, F., Lopatin, A., Chaikovsky, A., Torres, B., Derimian, Y., Huang, X., Aspetsberger, M., and Federspiel, C.: GRASP: a versatile algorithm for characterizing the atmosphere, SPIE Newsroom, https://doi.org/10.1117/2.1201408.005558, 2014.

Dubovik, O., Li, Z., Mishchenko, M. I., Tanré, D., Karol, Y., Bojkov, B., Cairns, B., Diner, D. J., Espinosa, W. R., Goloub, P., Gu, X., Hasekamp, O., Hong, J., Hou, W., Knobelspiesse, K. D., Landgraf, J., Li, L., Litvinov, P., Liu, Y., Lopatin, A., and Yin, D.: Polarimetric remote sensing of atmospheric aerosols: Instruments, methodologies, results, and perspectives, J. Quant. Spectrosc. Ra., 224, 474–511, https://doi.org/10.1016/j.jqsrt.2018.11.024, 2019.

Dubovik, O., Sinyuk, A., Lapyonok, T., Holben, B. N., Mishchenko, M., Yang, P., Eck, T. F., Volten, H., Muñoz, O., Veihelmann, B., van der Zande, W. J., Leon, J.-F., Sorokin, M., and Slutsker, I.: Application of spheroid models to account for aerosol particle nonsphericity in remote sensing of desert dust, J. Geophys. Res.-Atmos., 111, D11208 https://doi.org/10.1029/2005JD006619, 2006.

Escudero, M., Castillo, S., Querol, X., Avila, A., Alarcón, M., Viana, M. M., Alastuey, A., Cuevas, E., and Rodríguez, S.: Wet and dry African dust episodes over eastern Spain. J. Geophys. Res.-Atmos., 110, D18S08, https://doi.org/10.1029/2004JD004731, 2005.

Espinosa, W. R., Martins, J. V., Remer, L. A., Puthukkudy, A., Orozco, D., and Dolgos, G.: In situ measurements of angular-dependent light scattering by aerosols over the contiguous United States, Atmos. Chem. Phys., 18, 3737–3754, https://doi.org/10.5194/acp-18-3737-2018, 2018.

Espinosa, W. R., Remer, L. A., Dubovik, O., Ziemba, L., Beyersdorf, A., Orozco, D., Schuster, G., Lapyonok, T., Fuertes, D., and Martins, J. V.: Retrievals of aerosol optical and microphysical properties from Imaging Polar Nephelometer scattering measurements, Atmos. Meas. Tech., 10, 811–824, https://doi.org/10.5194/amt-10-811-2017, 2017.

European Union: Directive 2008/50/EC of the European Parliament and of the Council of 21 May 2008 on ambient air quality and cleaner air for Europe, https://eur-lex.europa.eu/eli/dir/2008/50/oj/eng (last access: 25 June 2025), 2008.

Fan, J., Wang, Y., Rosenfeld, D., and Liu, X.: Review of Aerosol–Cloud Interactions: Mechanisms, Significance, and Challenges, J. Atmos. Sci., 73, 4221–4252, https://doi.org/10.1175/JAS-D-16-0037.1, 2016.

Fernández, A. J., Sicard, M., Costa, M. J., Guerrero Rascado, J., Gomez, J., Molero, F., Barragán, R., Basart, S., Bortoli, D., Bedoya-Velásquez, A., Utrillas, M. P., Salvador, P., Granados-Muñoz, M. J., Potes, M., Ortiz-Amezcua, P., Martínez-Lozano, J. A., Artíñano, B., Muñoz-Porcar, C., Salgado, R., Román, R., Rocadenbosch, F., Salgueiro, V., Benavent-Oltra, J. A., Rodríguez-Gómez, A., Alados-Arboledas, L., Comerón, A., and Pujadas, M.: Extreme, wintertime Saharan dust intrusion in the Iberian Peninsula: lidar monitoring and evaluation of dust forecast models during the February 2017 event, Atmos. Res., 228, 223–241, https://doi.org/10.1016/j.atmosres.2019.06.007, 2019.

Floutsi, A. A., Baars, H., Engelmann, R., Althausen, D., Ansmann, A., Bohlmann, S., Heese, B., Hofer, J., Kanitz, T., Haarig, M., Ohneiser, K., Radenz, M., Seifert, P., Skupin, A., Yin, Z., Abdullaev, S. F., Komppula, M., Filioglou, M., Giannakaki, E., Stachlewska, I. S., Janicka, L., Bortoli, D., Marinou, E., Amiridis, V., Gialitaki, A., Mamouri, R.-E., Barja, B., and Wandinger, U.: DeLiAn – a growing collection of depolarization ratio, lidar ratio and Ångström exponent for different aerosol types and mixtures from ground-based lidar observations, Atmos. Meas. Tech., 16, 2353–2379, https://doi.org/10.5194/amt-16-2353-2023, 2023.

Formenti, P., Caquineau, S., Desboeufs, K., Klaver, A., Chevaillier, S., Journet, E., and Rajot, J. L.: Mapping the physico-chemical properties of mineral dust in western Africa: mineralogical composition, Atmos. Chem. Phys., 14, 10663–10686, https://doi.org/10.5194/acp-14-10663-2014, 2014.

Formenti, P., Elbert, W., Maenhaut, W., Haywood, J., and Andreae, M. O.: Chemical composition of mineral dust aerosol during the Saharan Dust Experiment (SHADE) airborne campaign in the Cape Verde region, September 2000, J. Geophys. Res.-Atmos., 108, 8576, https://doi.org/10.1029/2002jd002648, 2003.

Forster, P., Storelvmo, T., Armour, K., Collins, W., Dufresne, J.-L., Frame, D., Lunt, D. J., Mauritsen, T., Palmer, M. D., Watanabe, M., Wild, M., and Zhang, H.: The Earth's Energy Budget, Climate Feedbacks, A., and Climate Sensitivity, in: Climate Change 2021: The Physical Science Basis. Contribution of Working Group I to the Sixth Assessment Report of the Intergovernmental Panel on Climate Change, edited by: Masson-Delmotte, V., Zhai, P., Pirani, A., Connors, S.L., Péan, C., Berger, S., Caud, N., Chen, Y., Goldfarb, L., Gomis, M. I., Huang, M., Leitzell, K., Lonnoy, E., Matthews, J. B. R., Maycock, T. K., Waterfield, T., Yelekçi, O., Yu, T., and Zhou, B., Cambridge University Press, 953–1054, 2021.

GRASP-AirPhoton Multi-Angle Polarimeters (GAPMAP): Calibrated high information content measurements for atmospheric and surface products from a commercial constellation of cubesats, Vilamoura, Portugal, 16–20 May 2022, https://airdrive.eventsair.com/eventsairwesteuprod/production-atpi-public/cc816beb2ac8457f959951ce63947ebf, last access: 10 June 2025.

Gayet, J. F., Auriol, F., Oshchepkov, S., Schröder, F., Duroure, C., Febvre, G., Foumol, J. F., Crépel, O., Personne, P., and Daugereon, D.: In situ measurements of the scattering phase function of stratocumulus, contrails and cirrus, Geophys. Res. Lett., 25, 971–974, https://doi.org/10.1029/98GL00541, 1998.

Gómez Martín, J. C., Guirado, D., Frattin, E., Bermudez-Edo, M., Cariñanos Gonzalez, P., Olmo Reyes, F. J., Nousiainen, T., Gutiérrez, P. J., Moreno, F., and Muñoz, O.: On the application of scattering matrix measurements to detection and identification of major types of airborne aerosol particles: Volcanic ash, desert dust and pollen, J. Quant. Spectrosc. Ra., 271, 107761, https://doi.org/10.1016/j.jqsrt.2021.107761, 2021.

Gonçalves Ageitos, M., Obiso, V., Miller, R. L., Jorba, O., Klose, M., Dawson, M., Balkanski, Y., Perlwitz, J., Basart, S., Di Tomaso, E., Escribano, J., Macchia, F., Montané, G., Mahowald, N. M., Green, R. O., Thompson, D. R., and Pérez García-Pando, C.: Modeling dust mineralogical composition: sensitivity to soil mineralogy atlases and their expected climate impacts, Atmos. Chem. Phys., 23, 8623–8657, https://doi.org/10.5194/acp-23-8623-2023, 2023.

González-Flórez, C., Klose, M., Alastuey, A., Dupont, S., Escribano, J., Etyemezian, V., Gonzalez-Romero, A., Huang, Y., Kandler, K., Nikolich, G., Panta, A., Querol, X., Reche, C., Yus-Díez, J., and Pérez García-Pando, C.: Insights into the size-resolved dust emission from field measurements in the Moroccan Sahara, Atmos. Chem. Phys., 23, 7177–7212, https://doi.org/10.5194/acp-23-7177-2023, 2023.

González-Romero, A., González-Flórez, C., Panta, A., Yus-Díez, J., Reche, C., Córdoba, P., Moreno, N., Alastuey, A., Kandler, K., Klose, M., Baldo, C., Clark, R. N., Shi, Z., Querol, X., and Pérez García-Pando, C.: Variability in sediment particle size, mineralogy, and Fe mode of occurrence across dust-source inland drainage basins: the case of the lower Drâa Valley, Morocco, Atmos. Chem. Phys., 23, 15815–15834, https://doi.org/10.5194/acp-23-15815-2023, 2023.

Groß, S., Esselborn, M., Weinzierl, B., Wirth, M., Fix, A., and Petzold, A.: Aerosol classification by airborne high spectral resolution lidar observations, Atmos. Chem. Phys., 13, 2487–2505, https://doi.org/10.5194/acp-13-2487-2013, 2013.

Guerrero-Rascado, J. L., Olmo, F. J., Avilés-Rodríguez, I., Navas-Guzmán, F., Pérez-Ramírez, D., Lyamani, H., and Alados Arboledas, L.: Extreme Saharan dust event over the southern Iberian Peninsula in september 2007: active and passive remote sensing from surface and satellite, Atmos. Chem. Phys., 9, 8453–8469, https://doi.org/10.5194/acp-9-8453-2009, 2009.

Hasekamp, O., Litvinov, P., Fu, G., Chen, C., and Dubovik, O.: Algorithm evaluation for polarimetric remote sensing of atmospheric aerosols, Atmos. Meas. Tech., 17, 1497–1525, https://doi.org/10.5194/amt-17-1497-2024, 2024.

Haywood, J. and Boucher, O.: Estimates of the direct and indirect radiative forcing due to tropospheric aerosols: A review, Rev. Geophys., 38, 513–543, https://doi.org/10.1029/1999RG000078, 2000.

Holben, B. N., Eck, T. F., Slutsker, I., Tanré, D., Buis, J. P., Setzer, A., Vermote, E., Reagan, J. A., Kaufman, Y. J., Nakajima, T., Lavenu, F., Jankowiak, I., and Smirnov, A.: AERONET – A Federated Instrument Network and Data Archive for Aerosol Characterization, Remote Sens. Environ., 66, 1–16, https://doi.org/10.1016/S0034-4257(98)00031-5, 1998.

Holland, A. C. and Gagne, G.: The Scattering of Polarized Light by Polydisperse Systems of rregular Particles, Appl. Opt., 9, 1113–1121, https://doi.org/10.1364/AO.9.001113, 1970.

Horvath, H.: Extrapolation of a truncated aerosol volume scattering function to the far forward and back region, J. Aerosol Sci., 90, 26–35, https://doi.org/10.1016/j.jaerosci.2015.08.001, 2015.

Horvath, H., Alados Arboledas, L., and Olmo Reyes, F. J.: Angular scattering of the Sahara dust aerosol, Atmos. Chem. Phys., 18, 17735–17744, https://doi.org/10.5194/acp-18-17735-2018, 2018.

Hovenier, J. W., Volten, H., Muñoz, O., Van Der Zande, W. J., and Waters, L. B. F. M.: Laboratory studies of scattering matrices for randomly oriented particles: potentials, problems, and perspectives, J. Quant. Spectrosc. Ra., 79–80, 741–755, https://doi.org/10.1016/S0022-4073(02)00319-9, 2003.

Huang, Y., Kok, J. F., Martin, R. L., Swet, N., Katra, I., Gill, T. E., Reynolds, R. L., and Freire, L. S.: Fine dust emissions from active sands at coastal Oceano Dunes, California, Atmos. Chem. Phys., 19, 2947–2964, https://doi.org/10.5194/acp-19-2947-2019, 2019.

Huang, Y., Liu, C., Yao, B., Yin, Y., and Bi, L.: Scattering matrices of mineral dust aerosols: a refinement of the refractive index impact, Atmos. Chem. Phys., 20, 2865–2876, https://doi.org/10.5194/acp-20-2865-2020, 2020.

Jaggard, D., Hill, C., Stuart, D., Glantz, M., and Taggart, B.: Light scattering from particles of regular and irregular shape, Atmos. Environ., 15, 2511–2519, https://doi.org/10.1016/0004-6981(81)90066-4, 1981.

Järvinen, E., Kemppinen, O., Nousiainen, T., Kociok, T., Möhler, O., Leisner, T., and Schnaiter, M.: Laboratory investigations of mineral dust near-backscattering depolarization ratios, J. Quant. Spectrosc. Ra., 178, 192–208, https://doi.org/10.1016/j.jqsrt.2016.02.003, 2016.

Kahn, R., Banerjee, P., McDonald, D., and Diner, D. J.: Sensitivity of multiangle imaging to aerosol optical depth and to pure-particle size distribution and composition over ocean, J. Geophys. Res.-Atmos., 103, 32195–32213, https://doi.org/10.1029/98JD01752, 1988.

Kalnay, E., Kanamitsu, M., Kistler, R., Collins, W., Deaven, D., Gandin, L., Iredell, M., Saha, S., White, G., Woollen, J., Zhu, Y., Leetmaa, A., Reynolds, R., Chelliah, M., Ebisuzaki, W., Higgins, W., Janowiak, J., Mo, K. C., Ropelewski, C., Wang, J., Leetmaa, A., Reynolds, R., Jenne, R., and Joseph, D.: The NCEP/NCAR 40-Year Reanalysis Project, B. Am. Meteorol. Soc., 77, 437–471, https://doi.org/10.1175/1520-0477(1996)077<0437:TNYRP>2.0.CO;2, 1996.

Kanamitsu, M., Ebisuzaki, W., Woollen, J., Yang, S.-K., Hnilo, J. J., Fiorino, M., and Potter, G. L.: NCEP–DOE AMIP-II Reanalysis (R-2), B. Am. Meteorol. Soc., 83, 1631–1644, https://doi.org/10.1175/BAMS-83-11-1631, 2002.

King, M. D., Byrne, D. M., Herman, B. M., and Reagan, J. A.: Aerosol Size Distributions Obtained by Inversions of Spectral Optical Depth Measurements. J. Atmos. Sci., 35, 2153–2167, https://doi.org/10.1175/1520-0469(1978)035<2153:ASDOBI>2.0.CO;2, 1978.

Kok, J. F., Adebiyi, A. A., Albani, S., Balkanski, Y., Checa-Garcia, R., Chin, M., Colarco, P. R., Hamilton, D. S., Huang, Y., Ito, A., Klose, M., Leung, D. M., Li, L., Mahowald, N. M., Miller, R. L., Obiso, V., Pérez García-Pando, C., Rocha-Lima, A., Wan, J. S., and Whicker, C. A.: Improved representation of the global dust cycle using observational constraints on dust properties and abundance, Atmos. Chem. Phys., 21, 8127–8167, https://doi.org/10.5194/acp-21-8127-2021, 2021.

Kok, J. F., Ridley, D. A., Zhou, Q., Miller, R. L., Zhao, C., Heald, C. L., Ward, D. S., Albani, S., and Haustein, K.: Smaller desert dust cooling effect estimated from analysis of dust size and abundance, Nat. Geosci., 10, 274–278, https://doi.org/10.1038/ngeo2912, 2017.

Kok, J. F., Ward, D. S., Mahowald, N. M., and Evan, A. T.: Global and regional importance of the direct dust-climate feedback, Nat. Comm., 9, 241, https://doi.org/10.1038/s41467-017-02620-y, 2018.

Kuik, F., Stammes, P., and Hovenier, J. W.: Experimental determination of scattering matrices of water droplets and quartz particles, App. Opt., 30, 4872–4861, https://doi.org/10.1364/AO.30.004872, 1991.

Levy, R. C., Remer, L. A., Mattoo, S., Vermote, E. F., and Kaufman, Y. J.: Second-generation operational algorithm: Retrieval of aerosol properties over land from inversion of Moderate Resolution Imaging Spectroradiometer spectral reflectance, J. Geophys. Res.-Atmos., 112, D13211, https://doi.org/10.1029/2006JD007811, 2007.

Lyamani, H., Olmo, F. J., and Alados-Arboledas, L.: Light scattering and absorption properties of aerosol particles in the urban environment of Granada, Spain, Atmos. Environ., 42, 2630–2642, https://doi.org/10.1016/j.atmosenv.2007.10.070, 2008.

Lyamani, H., Olmo, F. J., and Alados-Arboledas, L.: Physical and optical properties of aerosols over an urban location in Spain: seasonal and diurnal variability, Atmos. Chem. Phys., 10, 239–254, https://doi.org/10.5194/acp-10-239-2010, 2010.

Lyamani, H., Fernández-Gálvez, J., Pérez-Ramírez, D., Valenzuela, A., Antón, M., Alados, I., Titos, G., Olmo, F. J., and Alados-Arboledas, L.: Aerosol properties over two urban sites in South Spain during an extended stagnation episode in winter season, Atmos. Environ., 62, 424–432, https://doi.org/10.1016/j.atmosenv.2012.08.050, 2012.

Manfred, K. M., Washenfelder, R. A., Wagner, N. L., Adler, G., Erdesz, F., Womack, C. C., Lamb, K. D., Schwarz, J. P., Franchin, A., Selimovic, V., Yokelson, R. J., and Murphy, D. M.: Investigating biomass burning aerosol morphology using a laser imaging nephelometer, Atmos. Chem. Phys., 18, 1879–1894, https://doi.org/10.5194/acp-18-1879-2018, 2018.

Meland, B., Kleiber, P. D., Grassian, V. H., and Young, M. A.: Correlated IR spectroscopy and visible light scattering measurements of mineral dust aerosol, J. Geophys. Res.-Atmos., 115, D20208, https://doi.org/10.1029/2010JD014389, 2010.

Miffre, A., Cholleton, D., Noël, C., and Rairoux, P.: Investigating the dependence of mineral dust depolarization on complex refractive index and size with a laboratory polarimeter at 180.0° lidar backscattering angle, Atmos. Meas. Tech., 16, 403–417, https://doi.org/10.5194/amt-16-403-2023, 2023.

Mischenko, M. I. and Travis, L. D.: Light scattering by polydispersions of randomly oriented spheroids with sizes comparable to wavelengths of observations, App. Opt., 33, 7206–7225, https://doi.org/10.1364/AO.33.007206, 1994.

Mischenko, M. I. and Travis, L. D.: Satellite retrieval of aerosol properties over the ocean using polarization as well as intensity of reflected sunlight, J. Geophys. Res., 102, 16989–17013, https://doi.org/10.1029/96JD02425, 1997.

Mischenko, M. I., Travis, L. D., and Lacis, A. A. Scattering, Absorption, and Emission of Light by Small Particles (First), Cambridge University Press, ISBN 978-0521782524, 2002.

Mishchenko, M. I., Cairns, B., Kopp, G., Schueler, C. F., Fafaul, B. A., Hansen, J. E., Hooker, R. J., Itchkawich, T., Maring, H. B., and Travis, L. D.: Accurate Monitoring of Terrestrial Aerosols and Total Solar Irradiance: Introducing the Glory Mission, B. Am. Meteorol. Soc., 88, 677–692, https://doi.org/10.1175/BAMS-88-5-677, 2007.

Moallemi, A., Modini, R. L., Brem, B. T., Bertozzi, B., Giaccari, P., and Gysel-Beer, M.: Concept, absolute calibration, and validation of a new benchtop laser imaging polar nephelometer, Atmos. Meas. Tech., 16, 3653–3678, https://doi.org/10.5194/amt-16-3653-2023, 2023.

Moallemi, A., Modini, R. L., Lapyonok, T., Lopatin, A., Fuertes, D., Dubovik, O., Giaccari, P., and Gysel-Beer, M.: Information content and aerosol property retrieval potential for different types of in situ polar nephelometer data, Atmos. Meas. Tech., 15, 5619–5642, https://doi.org/10.5194/amt-15-5619-2022, 2022.

Morcrette, J.-J., Boucher, O., Jones, L., Salmond, D., Bechtold, P., Beljaars, A., Benedetti, A., Bonet, A., Kaiser, J. W., Razinger, M., Schulz, M., Serrar, S., Simmons, A. J., Sofiev, M., Suttie, M., Tompkins, A. M., and Untch, A.: Aerosol analysis and forecast in the European Centre for Medium-Range Weather Forecasts Integrated Forecast System: Forward modeling, J. Geophys. Res.-Atmos., 114, D06206, https://doi.org/10.1029/2008JD011235, 2009.

Müller, D., Ansmann, A., Mattis, I., Tesche, M., Wandinger, U., Althausen, D., and Pisani, G.: Aerosol-type-dependent lidar ratios observed with Raman lidar, J. Geophys. Res.-Atmos., 112, D16202, https://doi.org/10.1029/2006JD008292, 2007.

Muñoz, O., Moreno, F., Guirado, D., Dabrowska, D. D., Volten, H., and Hovenier, J. W.: The Amsterdam–Granada Light Scattering Database, J. Quant. Spectrosc. Ra., 113, 565–574, https://doi.org/10.1016/j.jqsrt.2012.01.014, 2012.

Muñoz, O., Moreno, F., Guirado, D., Ramos, J. L., López, A., Girela, F., Jerónimo, J. M., Costillo, L. P., and Bustamante, I.: Experimental determination of scattering matrices of dust particles at visible wavelengths: The IAA light scattering apparatus, J. Quant. Spectrosc. Ra., 111, 187–196, https://doi.org/10.1016/j.jqsrt.2009.06.011, 2010a.

Muñoz, O., Volten, H., Hovenier, J. W., Nousiainen, T., Muinonen, K., Guirado, D., Moreno, F., and Waters, L. B. F. M.: Scattering matrix of large Saharan dust particles: Experiments and computations, J. Geophys. Res.-Atmos., 112, D13215, https://doi.org/10.1029/2006JD008074, 2007a.

Nakajima, T., Tonna, G., Rao, R., Boi, P., Kaufman, Y., and Holben, B.: Use of sky brightness measurements from ground for remote sensing of particulate polydispersions, App. Opt., 35, 2672, https://doi.org/10.1364/AO.35.002672, 1996.

Olmo, F. J., Quirantes, A., Alcántara, A., Lyamani, H., and Alados-Arboledas, L.: Preliminary results of a non-spherical aerosol method for the retrieval of the atmospheric aerosol optical properties, J. Quant. Spectrosc. Ra., 100, 305–314, https://doi.org/10.1016/j.jqsrt.2005.11.047, 2006.

Olmo, F. J., Quirantes, A., Lara, V., Lyamani, H., and Alados-Arboledas, L.: Aerosol optical properties assessed by an inversion method using the solar principal plane for non-spherical particles, J. Quant. Spectrosc. Ra., 109, 1504–1516, https://doi.org/10.1016/j.jqsrt.2007.12.019, 2008.

Ooki, A. and Uematsu, M.: Chemical interactions between mineral dust particles and acid gases during Asian dust events, J. Geophys. Res.-Atmos., 110, D03201, https://doi.org/10.1029/2004JD004737, 2005.

Párraga, J., Martín-García, J. M., Delgado, G., Molinero-García, A., Cervera-Mata, A., Guerra, I., Fernández-González, M. V., Martín-Rodríguez, F. J., Lyamani, H., Casquero-Vera, J. A., Valenzuela, A., Olmo, F. J., and Delgado, R.: Intrusions of dust and iberulites in Granada basin (Southern Iberian Peninsula). Genesis and formation of atmospheric iberulites, Atmos. Res., 248, 105260, https://doi.org/10.1016/j.atmosres.2020.105260, 2021.

Patrón, D., Lyamani, H., Titos, G., Casquero-Vera, J. A., Cardell, C., Močnik, G., Alados-Arboledas, L., and Olmo, F. J.: Monumental heritage exposure to urban black carbon pollution, Atmos. Environ., 170, 22–32, https://doi.org/10.1016/J.ATMOSENV.2017.09.030, 2017.

Pérez-Ramírez, D., Ruiz, B., Aceituno, J., Olmo, F. J., and Alados-Arboledas, L.: Application of Sun/star photometry to derive the aerosol optical depth, Int. J. Remote Sens., 29, 5113–5132, https://doi.org/10.1080/01431160802036425, 2008.

Pérez-Ramírez, D., Lyamani, H., Olmo, F. J., and Alados-Arboledas, L.: Improvements in star photometry for aerosol characterizations, J. Aerosol Sci., 42, 737–745, https://doi.org/10.1016/j.jaerosci.2011.06.010, 2011.

Pérez-Ramírez, D., Veselovskii, I., Whiteman, D. N., Suvorina, A., Korenskiy, M., Kolgotin, A., Holben, B., Dubovik, O., Siniuk, A., and Alados-Arboledas, L.: High temporal resolution estimates of columnar aerosol microphysical parameters from spectrum of aerosol optical depth by linear estimation: application to long-term AERONET and star-photometry measurements, Atmos. Meas. Tech., 8, 3117–3133, https://doi.org/10.5194/amt-8-3117-2015, 2015.

Pérez-Ramírez, D., Lyamani, H., Smirnov, A., O'Neill, N. T., Veselovskii, I., Whiteman, D. N., Olmo, F. J., and Alados-Arboledas, L.: Statistical study of day and night hourly patterns of columnar aerosol properties using sun and star photometry, Proc. SPIE 10001, Remote Sensing of Clouds and the Atmosphere XXI, 100010K, 19 October 2016, https://doi.org/10.1117/12.2242372, 2016.

Pérez-Ramírez, D., Whiteman, D. N., Veselovskii, I., Colarco, P., Korenski, M., and da Silva, A.: Retrievals of aerosol single scattering albedo by multiwavelength lidar measurements: Evaluations with NASA Langley HSRL-2 during discover-AQ field campaigns, Remote Sens. Environ., 222, 144–164, https://doi.org/10.1016/j.rse.2018.12.022, 2019.

Perry, R. J., Hunt, A. J., and Huffman, D. R.: Experimental determinations of Mueller scattering matrices for nonspherical particles, Appl. Opt., 17, 2700–2710, https://doi.org/10.1364/AO.17.002700, 1978.

Petzold, A. and Schönlinner, M.: Multi-angle absorption photometry – a new method for the measurement of aerosol light absorption and atmospheric black carbon, J. Aerosol Sci., 35, 421–441, https://doi.org/10.1016/J.JAEROSCI.2003.09.005, 2004.

Pope, S. K., Tomasko, M. G., Williams, M. S., Perry, M. L., Doose, L. R., and Smith, P. H.: Clouds of Ammonia Ice: Laboratory Measurements of the Single-Scattering Properties, ICARUS, 100, 203–220, https://doi.org/10.1016/0019-1035(92)90030-B, 1992.

Querol, X., Pérez, N., Reche, C., Ealo, M., Ripoll, A., Tur, J., Pandolfi, M., Pey, J., Salvador, P., Moreno, T., and Alastuey, A.: African dust and air quality over Spain: Is it only dust that matters?, Sci. Total Environ., 686, 737–752, https://doi.org/10.1016/j.scitotenv.2019.05.349, 2019.

Remer, L. A., Davis, A. B., Mattoo, S., Levy, R. C., Kalashnikova, O. V., Coddington, O., Chowdhary, J., Knobelspiesse, K., Xu, X., Ahmad, Z., Boss, E., Cairns, B., Dierssen, H. M., Diner, D. J., Franz, B., Frouin, R., Gao, B.-C., Ibrahim, A., Martins, J. V., Omar, A. H., Torres, O., Xu, F., and Zhai, P.-

W.: Retrieving Aerosol Characteristics From the PACE Mission, Part 1: Ocean Color Instrument, Front. Earth Sci., 7, 152, https://doi.org/10.3389/feart.2019.00152, 2019.

Renard, J.-B., Dulac, F., Durand, P., Bourgeois, Q., Denjean, C., Vignelles, D., Couté, B., Jeannot, M., Verdier, N., and Mallet, M.: In situ measurements of desert dust particles above the western Mediterranean Sea with the balloon-borne Light Optical Aerosol Counter/sizer (LOAC) during the ChArMEx campaign of summer 2013, Atmos. Chem. Phys., 18, 3677–3699, https://doi.org/10.5194/acp-18-3677-2018, 2018.

Renard, J. B., Hadamcik, E., Couté, B., Jeannot, M., and Levasseur-Regourd, A. C.: Wavelength dependence of linear polarization in the visible and near infrared domain for large levitating grains (PROGRA2 instruments), J. Quant. Spectrosc. Ra., 146, 424–430, https://doi.org/10.1016/j.jqsrt.2014.02.024, 2014.

Renard, J.-B., Francis, M., Hadamcik, E., Daugeron, D., Couté, B., Gaubicher, B., and Jeannot, M.: Scattering properties of sands. 2. Results for sands from different origins, App. Opt., 40, 3352–3559, https://doi.org/10.1364/AO.49.003552, 2010.

Renard, J.-B., Hadamcik, E., Worms, J.-C., and Hadamcik, E.: The laboratory PROGRA2 database to interpret the linear polarization and brightness phase curves of light scattered by solid particles in clouds and layers, J. Quant. Spectrosc. Ra., 320, 108980, https://doi.org/10.1016/j.jqsrt.2024.108980, 2024.

Rodríguez, S. and López-Darias, J.: Extreme Saharan dust events expand northward over the Atlantic and Europe, prompting record-breaking PM_{10} and $PM_{2.5}$ episodes, Atmos. Chem. Phys., 24, 12031–12053, https://doi.org/10.5194/acp-24-12031-2024, 2024.

Rodrıguez, S., Querol, X., Alastuey, A., Kallos, G., and Kakaliagou, O.: Saharan dust contributions to PM_{10} and TSP levels in Southern and Eastern Spain, Atmos. Environ., 35, 2433–2447, https://doi.org/10.1016/S1352-2310(00)00496-9, 2001.

Rosenfeld, D., Andreae, M. O., Asmi, A., Chin, M., de Leeuw, G., Donovan, D. P., Kahn, R., Kinne, S., Kivekäs, N., Kulmala, M., Lau, W., Schmidt, K. S., Suni, T., Wagner, T., Wild, M., and Quaas, J.: Global observations of aerosol-cloud-precipitation-climate interactions, Rev. Geophys., 52, 750–808, https://doi.org/10.1002/2013RG000441, 2014.

Saito, M. and Yang, P.: Advanced bulk optical models linking the backscattering and microphysical properties of mineral dust, Geophys. Res. Lett., 48, e2021GL095121, https://doi.org/10.1029/2021GL095121, 2021.

Saito, M., Yang, P., Ding, J., and Liu, X.: A comprehensive database of the optical properties of irregular aerosol particles for radiative transfer simulations, J. Atmos. Sci., 78, 2089–2111, https://doi.org/10.1175/JAS-D-20-0338.1, 2021.

Saito, M. and Yang, P.: Quantifying the impact of the surface roughness of hexagonal ice crystals on backscattering properties for lidar-based remote sensing applications, Geophys. Res. Lett., 50, e2023GL104175, https://doi.org/10.1029/2023GL104175, 2023.

Sakai, T., Nagai, T., Zaizen, Y., and Mano, Y.: Backscattering linear depolarization ratio measurements of mineral, sea-salt, and ammonium sulfate particles simulated in a laboratory chamber, App. Opt., 49, 4441–4449, https://doi.org/10.1364/AO.49.004441, 2010.

Salvador, P., Alonso-Pérez, S., Pey, J., Artíñano, B., de Bustos, J. J., Alastuey, A., and Querol, X.: African dust outbreaks over the western Mediterranean Basin: 11-year characterization of atmospheric circulation patterns and dust source areas, Atmos. Chem. Phys., 14, 6759–6775, https://doi.org/10.5194/acp-14-6759-2014, 2014.

Schmeisser, L., Andrews, E., Ogren, J. A., Sheridan, P., Jefferson, A., Sharma, S., Kim, J. E., Sherman, J. P., Sorribas, M., Kalapov, I., Arsov, T., Angelov, C., Mayol-Bracero, O. L., Labuschagne, C., Kim, S.-W., Hoffer, A., Lin, N.-H., Chia, H.-P., Bergin, M., Sun, J., Liu, P., and Wu, H.: Classifying aerosol type using in situ surface spectral aerosol optical properties, Atmos. Chem. Phys., 17, 12097–12120, https://doi.org/10.5194/acp-17-12097-2017, 2017.

Teri, M., Gasteiger, J., Heimerl, K., Dollner, M., Schöberl, M., Seibert, P., Tipka, A., Müller, T., Aryasree, S., Kandler, K., and Weinzierl, B.: Pollution affects Arabian and Saharan dust optical properties in the Eastern Mediterranean, EGUsphere [preprint], https://doi.org/10.5194/egusphere-2024-701, 2024.

Titos, G., del Águila, A., Cazorla, A., Lyamani, H., Casquero-Vera, J. A., Colombi, C., Cuccia, E., Gianelle, V., Močnik, G., Alastuey, A., Olmo, F. J., and Alados-Arboledas, L.: Spatial and temporal variability of carbonaceous aerosols: Assessing the impact of biomass burning in the urban environment, Sci. Total Environ., 578, 613–625, https://doi.org/10.1016/j.scitotenv.2016.11.007, 2017.

Titos, G., Lyamani, H., Pandolfi, M., Alastuey, A., and Arboledas, L.: Identification of fine (PM_1) and coarse (PM_{10-1}) sources of particulate matter in an urban environment, Atmos. Environ., 89, 593–602, https://doi.org/10.1016/j.atmosenv.2014.03.001, 2014.

Torres, B., Dubovik, O., Fuertes, D., Schuster, G., Cachorro, V. E., Lapyonok, T., Goloub, P., Blarel, L., Barreto, A., Mallet, M., Toledano, C., and Tanré, D.: Advanced characterisation of aerosol size properties from measurements of spectral optical depth using the GRASP algorithm, Atmos. Meas. Tech., 10, 3743–3781, https://doi.org/10.5194/amt-10-3743-2017, 2017.

Valenzuela, A., Olmo, F. J., Lyamani, H., Antón, M., Quirantes, A., and Alados-Arboledas, L.: Aerosol radiative forcing during African desert dust events (2005–2010) over Southeastern Spain, Atmos. Chem. Phys., 12, 10331–10351, https://doi.org/10.5194/acp-12-10331-2012, 2012a.

Valenzuela, A., Olmo, F. J., Lyamani, H., Antón, M., Quirantes, A., and Alados-Arboledas, L.: Classification of aerosol radiative properties during African desert dust intrusions over southeastern Spain by sector origins and cluster analysis, J. Geophys. Res.-Atmos., 117, D06214, https://doi.org/10.1029/2011JD016885, 2012b.

Valenzuela, A., Olmo, F. J., Lyamani, H., Antón, M., Titos, G., Cazorla, A., and Alados-Arboledas, L.: Aerosol scattering and absorption Angström exponents as indicators of dust and dust-free days over Granada (Spain), Atmos. Res., 154, 1–13, https://doi.org/10.1016/j.atmosres.2014.10.015, 2015.

Valenzuela, A., Olmo, F. J., Lyamani, H., Granados-Muñoz, M. J., Antón, M., Guerrero-Rascado, J. L., Quirantes, A., Toledano, C., Perez-Ramírez, D., and Alados-Arboledas, L.: Aerosol transport over the western mediterranean basin: Evidence of the contribution of fine particles to desert dust plumes over alborán island, J. Geophys. Res., 119, 14028–14044, https://doi.org/10.1002/2014JD022044, 2014.

Volten, H., Muñoz, O., Rol, E., De Haan, J. F., Vassen, W., Hovenier, J. W., Muinonen, K., and Nousiainen, T.: Scattering matrices of mineral aerosol particles at 441.6 nm and 632.8 nm, J. Geophys. Res.-Atmos., 106, 17375–17401, https://doi.org/10.1029/2001JD900068, 2001.

West, R. A., Doose, L. R., Eibl, A. M., Tomasko, M. G., and Mishchenko, M. I.: Laboratory measurements of mineral dust scattering phase function and linear polarization, J. Geophys. Res.-Atmos., 102, 16871–16881, https://doi.org/10.1029/96jd02584, 1997.

Wyatt, P. J., Schehrer, K. L., Phillips, S. D., Jackson, C., Chang, Y.-J., Parker, R. G., Phillips, D. T., and Bottiger, J. R.: Aerosol particle analyzer, App. Opt., 27, 217–221, https://doi.org/10.1364/AO.27.000217, 1988.

Zhang, X., Dai, C., Wei, H., Liu, J., Li, W., Wu, K., and Zou, S.: Optical properties of mineral dust aerosols with non-absorptive coating: A numerical investigation, J. Quant. Spectrosc. Ra., 302, 108564, https://doi.org/10.1016/j.jqsrt.2023.108564, 2023.

Zhang, X., Wei, H., Zou, S., Duan, J., Li, W., and Dai, C.: Effect of nitrate coatings on the optical properties of mineral dust particles during the haze aging process, J. Quant. Spectrosc. Ra., 277, 107966, https://doi.org/10.1016/j.jqsrt.2021.107966, 2022.